AFRL-VS-HA-TR-2004-1166

DTIC COPY

QUANTIFYING SOURCE EXCITATION AND PATH EFFECTS FOR HIGH FREQUENCY REGIONAL WAVES

Ru-Shan Wu
Xiao-Bi-Xie
Thorne Lay

Institute of Geophysics and Planetary Physics
University of California, Santa Cruz
1156 High Street
Santa Cruz, CA 95064

1 October 2004

Final Report

20050308 032

AIR FORCE RESEARCH LABORATORY
Space Vehicles Directorate
29 Randolph Rd
AIR FORCE MATERIEL COMMAND
Hanscom AFB, MA 01731-3010

This technical report has been reviewed and is approved for publication.

ROBERT RAISTRICK
Contract Manager

ROBERT BELAND
Branch Chief

REPORT DOCUMENTATION PAGE

1. REPORT DATE (DD-MM-YYYY)	2. REPORT TYPE	3. DATES COVERED (From - To)
01-10-2004	FINAL	1 Oct 2001 – 30 Sep 2004

4. TITLE AND SUBTITLE
Quantifying Source Excitation and Path Effects For High Frequency Regional Waves

5a. CONTRACT NUMBER
DTRA01-01-C-0076

5b. GRANT NUMBER

5c. PROGRAM ELEMENT NUMBER

6. AUTHOR(S)
Ru-Shan Wu, Xiao-Bi Xie, and Thorne Lay

5d. PROJECT NUMBER
DTRA

5e. TASK NUMBER
OT

5f. WORK UNIT NUMBER
A1

7. PERFORMING ORGANIZATION NAME(S) AND ADDRESS(ES)

Institute of Geophysics and Planetary Physics
University of California, Santa Cruz
1156 High Street
Santa Cruz, CA 95064

8. PERFORMING ORGANIZATION REPORT NUMBER

9. SPONSORING / MONITORING AGENCY NAME(S) AND ADDRESS(ES)
Air Force Research Laboratory
29 Randolph Road
Hanscom AFB, MA 01731-3010

Contract Manager: R. Raistrick AFRL/VSBYE

10. SPONSOR/MONITOR'S ACRONYM(S)
AFRL

11. SPONSOR/MONITOR'S REPORT NUMBER(S)
AFRL-VS-HA-TR-2004-1166

12. DISTRIBUTION / AVAILABILITY STATEMENT
Approved for Public Release; Distribution Unlimited.

13. SUPPLEMENTARY NOTES

14. ABSTRACT

This research is directed at investigation of regional wave excitation and propagation in complicated crustal waveguides using numerical simulations. The report covers three major approaches: (1) A finite-difference plus slowness analysis method for investigating near-source Lg-wave excitation and partitioning; (2) The half-space screen method for simulating high frequency Lg-wave propagation; and (3) A boundary element method for calculating Lg-wave propagation in the crustal waveguide with uneven surface topography.

15. SUBJECT TERMS

Seismic wave propagation, Lg-wave, CTBT, Numerical simulation

16. SECURITY CLASSIFICATION OF:

a. REPORT	b. ABSTRACT	c. THIS PAGE	17. LIMITATION OF ABSTRACT	18. NUMBER OF PAGES	19a. NAME OF RESPONSIBLE PERSON
UNCLAS	UNCLAS	UNCLAS	SAR		Robert J. Raistrick

19b. TELEPHONE NUMBER (include area code)
781-377-3726

Standard Form 298 (Rev. 8-98)
Prescribed by ANSI Std. 239.18

ABSTRACT

This research is directed at investigation of regional wave excitation and propagation in complicated crustal waveguide using numerical simulations. The report covers three major approaches: a finite-difference plus slowness analysis method for investigating near-source Lg-wave excitation and partitioning; the half-space screen method for simulating high frequency Lg-wave propagation; and a boundary element method for calculating Lg-wave propagation in a crustal waveguide with surface topography.

(1) A finite-difference modeling plus slowness analysis method is developed to investigate the near source Lg-wave excitation and energy partitioning. The method allows a very fine structure to be used for simulating the near-source processes. The slowness analysis is used for tracking where energy will be partitioned into the long-range propagation regime. The high efficiency of the method allows the examination of many source-model combinations. The near source P-to-S conversion in the presence of small-scale random heterogeneities is tested as a mechanism for generating the near source S-wave energy from an explosive source. The numerical results reveal that the depth of the source and the depth of the scattering region have strong effects on the P-to-S conversion and the partitioning of energy into trapped and leaking signal. The excitation spectrum for the trapped energy from the S*-wave is also investigated. The modeling shows that the excitation is generally favorable for lower frequencies and shallow source depth. We simulate the amplitude ratio between the P- and trapped S-waves for a relatively broad frequency range using velocity models with and without lateral velocity variations. For a typical explosion source and a shallow earthquake source the results show a general behavior similar to that of the observations.

(2) The half-space screen method has been further improved to model Lg-wave propagation in the complex crustal waveguides, including irregular topography, large-scale geological structures and small-scale random heterogeneities. The screen method has been extended to the P-SV case. Both P- and S-wave quality factors are incorporated into P-SV and SH-wave propagators to handle the effects of intrinsic attenuation on regional Lg. The resulting propagator provides a useful tool for investigating the relationship between Lg wave attenuation and crustal waveguide properties. Different attenuation mechanisms including intrinsic attenuation, leakage due to rough topography and Moho discontinuity, and scattering attenuation due to small-scale random heterogeneities are tested and investigated separately. Then, their combined effects on Lg-wave propagation in near-realistic crustal waveguides are estimated and the corresponding apparent Lg quality factors are calculated. The synthetic apparent Lg Q and its frequency dependence fall into the range of actual observations.

(3) An indirect boundary element method is developed to calculate the two-dimensional P-SV elastic response for crustal waveguide model. The method allows us to accurately handle the wave propagation in models with irregular topography. The validity and accuracy of the method are checked by comparing the boundary element calculations with the results from other numerical methods. Numerical simulations with this scheme show that rough topography can scatter the P and Rayleigh wave and attenuate the energy propagation in the waveguide. In order to simulate long-range high-frequency propagation of regional waves and to avoid calculating huge matrixes, a connection technique is proposed and tested. Using the technique, a long

waveguide can be divided into relatively short sections, and the boundary element method can be used section by section to calculate the effect of rough topography on wave propagation at extended regional distances.

TABLE OF CONTENTS

1. RESEARCH OBJECTIVES

With the current emphasis on global monitoring for low-yield nuclear tests, regional seismic phases such as Lg and Lg coda have become very important for magnitude and yield estimation of underground nuclear tests. (e.g., Nuttli, 1986; Xie, et al., 1996; Patton, 2001). In addition, various P/S-type amplitude ratios for high frequency regional phases (e.g., Pn/Sn, Pn/Lg, Pg/Lg, Pg/Sn) have become important for event discrimination (e.g., Taylor et al., 1989; Kim et al., 1993, 1997; Walter et al., 1995; Fisk et al., 1996; Taylor, 1996; Taylor and Hartse, 1997; Hartse et al., 1997; Fan and Lay, 1998a-c; Xie and Patton, 1999). The applications of regional phases for yield estimation and event discrimination are largely based on empirical approaches, and while very promising in many cases, there is great need for quantification of how and why they work, and equally importantly, how and why they may fail under certain circumstances. These questions are closely related to the Lg wave excitation and propagation. Due to the complex processes involved, it is difficult to separate the contribution of individual mechnisms from the observed data empirically. Numerical modeling approaches are thus of great importance for investigating the excitation and propagation of regional phases.

A major goal of the UCSC Regional Wave Synthetic Seismogram research program is to develop computationally viable techniques for investigating the excitation and path effects for high-frequency regional waves. The techniques that have been developed include: (1) The finite-difference simulation combined with slowness analysis method (Xie and Lay, 1994; Wu, et al. 2002, 2003, 2004), which is targeted to investigate the near-source energy partitioning for regional phases. (2) The generalized screen propagator (GSP) method (Wu, 1994, 1996; Wu, Jin and Xie, 1996, 2000a, b; Xie and Wu, 2001; Wu and Wu, 2001; Wu, et al., 1998, 1999, 2000). This method handles laterally varying crustal structures including volumetric heterogeneities, intrinsic attenuation and rough free surface. Under one-way wave equation theory, it is highly suited for investigating high frequency and long distance regional wave propagation. (3) The boundary element method (Fu and Wu, 2000, 2001; Fu, et al., 2002; Wu, et al. 2003). This method can accurately handle uneven surface topography and interfaces with strong impedance contrasts and is suitable for investigating interactions between waves and discontinuities. These numerical tools teamed together enable the simulation of the entire regional wave excitation and propagation processes.

2. LG-WAVE EXCITATION AND NEAR-SOURCE ENERGY PARTITIONING

2.1 Background

For explosion sources, there are major questions about the nature of excitation of S-wave dominated phases such as Lg, and there are similar questions regarding the relative excitation effects for P/S-type ratios in regional phases, particularly given the huge scatter observed in both earthquake and explosion data populations. Several possible near source energy transfer mechanisms have been proposed, including P- Lg scattering, pS-Lg conversion at the free surface, Rg-to-Lg coupling, S*-Lg conversion, spall excitation of S, tectonic release and rock-damage (e.g., Day and Mclaughlin, 1991; Gupta et al., 1992, 1997; Wallace, 1991; Gutowski, et al., 1984; Vogfjord, 1997; Johnson and Sammis, 2001). There is continuing controversy about which mechanism(s) dominate the explosion source energy partitioning processes. Recent observations from the DOB experiment at the Shagan Test Site provide evidence that the shallow source exhibits increased S-wave excitation, which supports the Rg-to-Lg conversion hypothesis (Myers, et al., 2003; Bonner, et al., 2003). However, other evidence suggests that the S-wave may be generated primarily by the nonspherical part of the explosion source, with strong influence from the free surface (Stevens, et al., 2003). Another unsolved puzzle is the frequency dependence observed for regional P/S discriminants. Numerous studies (e.g., Walter et al., 1995; Fisk et al., 1996; Taylor, 1996; Taylor and Hartse, 1997; Hartse et al., 1997; Fan et al., 2002) have demonstrated that regional P/S measurements (Pn/Lg, Pg/Lg, Pn/Sn, Pg/Sn) provide useful discrimination of earthquakes and explosions at frequencies above about 3 Hz, but the discrimination performance is much lower at low frequencies. There is very incomplete theoretical understanding of this strong frequency-dependent phenomenon.

Early numerical simulations investigated various propagation properties of the Lg phase using the wavenumber integral method (e.g., Bouchon, 1982; Campillo et al., 1984; Campillo and Paul, 1992). These works revealed many propagation and excitation characteristics of regional phases in horizontally stratified crustal models. However, with a 1D model, many phenomena linked to the laterally varying crustal heterogeneity cannot be generated so the results were very limited.

Using full wave numerical techniques such as finite-difference (FD) (Frankel 1986; Vidale and Helmberger, 1988; Hayashi, et al., 2001) or pseudo spectrum methods (Kosloff and Baysal, 1982; Tessmer and Kosloff, 1994; Orrey, et al., 2003) to explore seismic wave propagation has the advantage that complicated two- or three-dimensional structures can be included in the model and the complete wave field can be calculated. These numerical methods are also widely used for investigating Lg-wave excitation and propagation in complicated crustal waveguides. Xie and Lay (1994) investigated Lg-wave excitation using the FD method. Jih (1995, 1996) investigated Rg-to-Lg coupling as a possible Lg excitation mechanism. Using 2D and 3D general Fourier method, Bonner, et al. (2003) investigated Rg and Lg generation, and partially reproduced the observed spectrum from the Depth of Burial Experiment. Stevens et al. (2003) investigated the physical basis of explosion generated S-waves using a 2D nonlinear FD method, which handles axisymmetric near source effects including spall, cracking, and nonlinear deformation.

The main disadvantages of these numerical methods that provide complete synthetic seismograms are the low computation efficiency and huge computer memory requirement, especially when applied to investigate the characteristics of Lg excitation. For the purpose of

small nuclear test monitoring, the range of interest for Lg-wave simulation involves a broad frequency band (0.2 to 10 Hz) and long propagation distances (up to 1000 km or more). At the same time, the factors that control the source energy partitioning depend on the detailed source mechanism and fine near source velocity structure. In addition, there are multiple mechanisms that may potentially contribute to the energy partitioning process. Numerous parameters need to be tested to investigate the characteristics of these mechanisms, especially their contributions to the frequency dependent features of observable discriminants. If random heterogeneities are to be considered, as is likely to be important for high frequency signals, the results have to be calculated statistically from simulations using a large number of realizations. This limits the approach of complete FD synthesis for actually recording geometries.

Although there are continuing controversies about the dominant P-to-S transfer mechanisms affecting regional phases, most investigators agree that appreciable energy from explosion sources is converted to S-waves in the near-source region (Myers, 2003). The physical processes by which an explosion source generates regional phases can be described as energy partitioning taking place in the near-source region. The partitioned energy subsequently propagates through a long waveguide, where secondary energy partitioning effects may take place, but these are less associated with the type of source involved. The combined processes in the near-source region and along the path naturally separate the wave field energy into groups of observable regional phases according to their slowness and group velocity. If the propagation effect is not the primary goal of an investigation, there is a strategy to avoid calculating the immensely time-consuming long distance propagation part of the problem, focusing on the near-source energy partitioning effects. Based on this concept, we developed a method based on the finite-difference simulation and slowness analysis to investigate the near-source energy partitioning of an explosion source. This method investigates the partitioning process right at the source region. The localized analysis thereby provides uncontaminated information isolating the physical processes controlling the energy partitioning.

2.2 Methodology

Many authors (e.g. Frankel, 1989; Xie and Lay, 1994; Vogfjord, 1997) have pointed out that for S-wave energy to be trapped in the waveguide reverberating to generate the Lg-wave, it must propagate with post critical angle at the Moho discontinuity. However, in the waveguide and especially in the near-source region, the wavefield is highly complicated. It is impractical to trace each phase in the spatial-time domain. An alternate, but equally valid way of tracking the wave energy is in the slowness domain. Multiply-reflected waves may arrive simultaneously in time, but in the slowness domain their energy distribution gives clear information about the wave intensity, slowness and propagation direction. Several methods can be used to transfer spatial-time domain data into slowness (or equivalently wavenumber) domain information, for example, FK analysis or beamforming (slant stacking). Here we employ the slant stack method, but with the novelty that we use localized slowness analysis, working simultaneously on both space and slowness domain. Based on this method (introduced by Xie and Lay, 1994 and further developed by Wu et al., 2002, 2003), the wave field at short distance is sampled with different spatial, time and frequency windows. Then the energy is characterized as a function of phase velocity based on the slowness analysis. The output provides localized information in time,

space, frequency and slowness domains, which provides the overall information for investigating the characteristics of energy partitioning.

Figure 2.1 illustrates the basic concept of the finite-difference simulation plus slowness analysis (FDSA) method for investigating the near-source Lg-wave excitation and energy partitioning. In Figure 2.1, (A) shows the finite-difference simulation snap-shot extended out to regional distances where internal waveguide slowness analysis can be conducted as well as where surface theoretical seismograms can be computed; (B) is the near source model composed of different types of source representations and fine near source structures that can be used to test different energy partitioning mechanisms; (C) is a summary of the slowness analysis which sorts the energy from the short distance array data and predicts the trapped waveguide energy at larger distances.
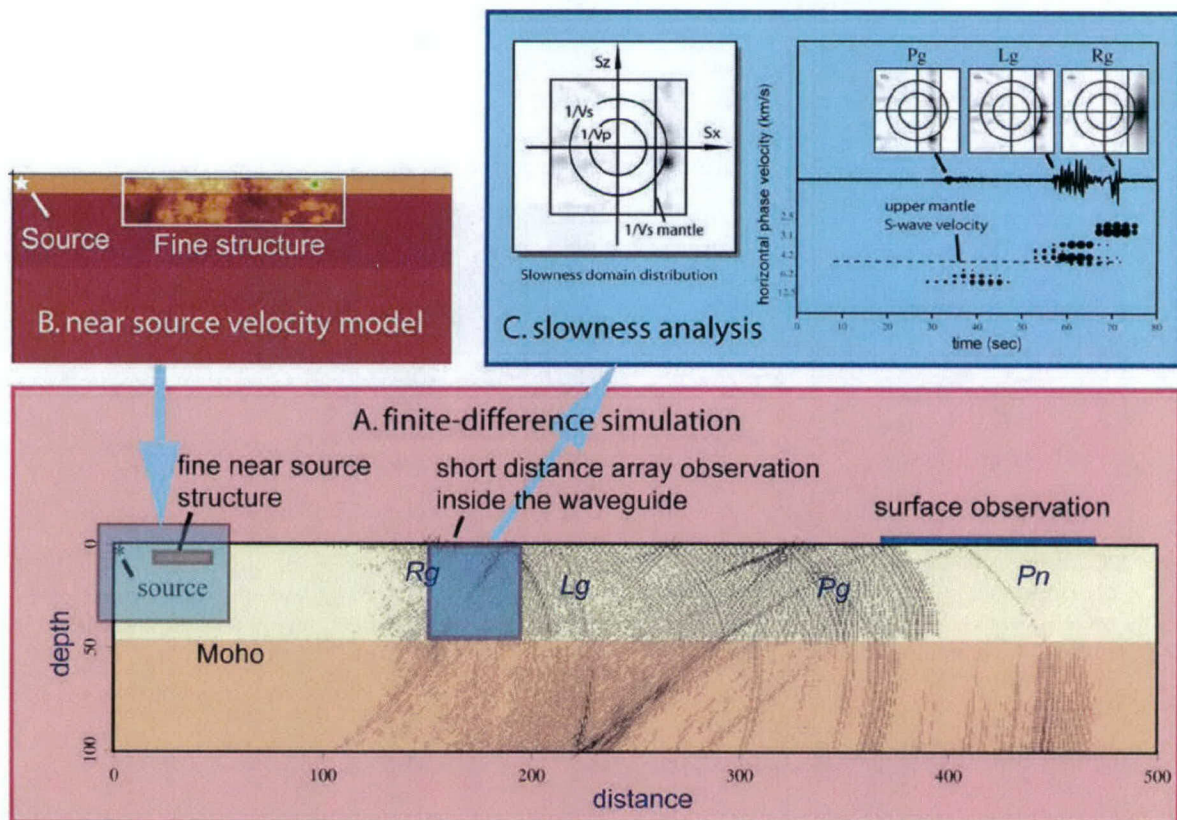
Figure 2.1. Cartoon showing the finite-difference simulation and slowness analysis method. (A) The finite-difference modeling used to propagate the wavefield within the crustal waveguide is illustrated by a snap-shot of the displacement field. (B) Fine near source velocity model used to investigate near source energy partitioning. (C) Energy flux at the short distance is calculated and used to predict the long distance observations. These predictions are corroborated by analysis of surface sythetics at large distances.

Figure 2.2 shows different energy distributions for slowness analysis. The energy can either be expressed as a function in slowness domain, or as a function in mixed slowness-depth domain. The measurement can be made in the entire cross section of the waveguide. The upper mantle S-

9

wave slowness $1/v_{S-mantle}$ is marked for different cases. All S-wave energy (either directly radiated from the source or converted from other wave types) with apparent horizontal slowness larger than the upper mantle S-wave slowness will be trapped in the crustal waveguide and will contribute to the guided S phase unless subsequent scattering causes it to leak out. Effectively, the relative amplitude of the trapped S-wave energy can be determined at a short distance. The strength of these S-waves will depend on two factors, the intensity of the S energy radiated or converted in the near-source region, as well as the percentage of the energy that can intrinsically be trapped in the waveguide. The slowness analysis is done within spatial, time and frequency windows. The localized slowness analysis allows the energy flux in the waveguide to be investigated in mixed domains of space, travel-time, slowness, and frequency. The energy distribution in these joint domains has a better chance of being separated than in conventional seismogram analyses, and the underlying physical mechanisms controlling the energy partitioning can thus be investigated.
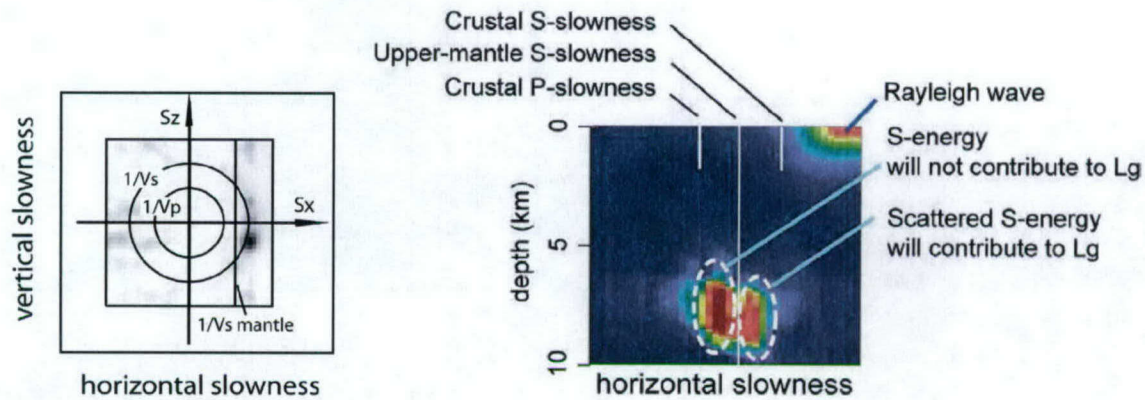
Figure 2.2. Slowness domain display. Left: energy distribution in 2D slowness domain, right: energy distribution in mixed horizontal slowness-depth domain. Vertical lines indicate the upper-mantle S-wave slowness. Energy falling on the right-hand side of these lines will be trapped in the waveguide and will form guided S phases like Lg.

2.3 Verification of the method

To verify our method, we computed a suite of large 2D FD simulations (see Figure 2.1). For all numerical examples calculated in this report, we will use the EK (Eastern Kazakh) model (Priestley et al., 1988) as the background and modify it by adding different laterally varying structures. A range of sources and near-source structures were used in the simulations. Surface receivers at long distance are computed to provide conventional regional phase synthetics that we treat as distant observations of the wave field. Vertical arrays embedded in the crustal waveguide at short distances are used for the slowness analysis.

Figure 2.3 shows the results for a cross section at 180 km in the crustal waveguide. In each panel, the vertical axis is the horizontal slowness. The horizontal axis is time. The group velocity

is also marked on the top of each panel. The dashed line marks the upper mantle S-wave velocity. The solid circles are energy picked from the slowness domain and summed up for the entire cross section. The left column is for low frequency (0.3 -1.5 Hz) and the right column is for high-frequency (2.0-5.0 Hz). The top panel is for background velocity model. It is important to note that the Rg mainly appears as a low-frequency signal and the Pg mainly appears as the high-frequency signal. We first focus on the low frequency results. From the top panel we can see Pg-wave and strong fundamental mode Rg-wave. However, such a high velocity crust generates very poor Lg-waves. Within the Lg wave window, only very weak energy can be observed which may result from the S*-wave. In the second panel, a random velocity patch located at depth 0.0-2.5 km is added to the background model (refer to Figure 2.1). Compared with the background model, through scattering, the Rg-wave loses considerable energy while the Lg-wave gains energy. Panels 3 to 5 are similar to panel 2, except random patches are located at depths 2.5-5.0 km, 5.0-7.5 km and 10.0-12.5 km, respectively. The tendency is: the shallower the random patch the more energy is transferred. This also provides additional evidence that the low frequency Lg energy may come from the Rg-wave, since the Rg energy is mostly concentrated at the shallow depth.

Figure 2.4 shows the comparison between waveguide energy flux at 180 km calculated using slowness analysis (left panel) and at 450 km calculated from the surface measurement using conventional Lg wave processing technique (right panel). For simplicity, we label the predictions of trapped energy as "Lg" energy. Several random velocity patches are incorporated in the near-source region to provide the wave field coupling. The vertical extent of the patches is 2.5 km, with RMS velocity fluctuation of 10% and the positioning of the patches varies from 0 to 15 km in depth. The results show the relative energy changes (short color bars) of Pg-, Lg- and Rg-waves, as functions of the depth range of the random velocity scattering patch for each case. The thin lines indicate the reference energy level for a velocity model without any random velocity scattering patch. Short color bars indicate the energy changes due to the near source scattering at different depths. These calculations demonstrate that the relative changes of energy for each of these phases obtained in the waveguide slowness analysis correspond very closely to those obtained on the free surface at long distance, even for dramatic changes such as the strong scattering of Rg which occurs when the scattering patch is just below the surface. These calculations confirm that the near-source slowness analysis within the waveguide correctly predicts the surface regional observations at greater distance; this is the heart of our strategy.

To examine the energy flux measurements obtained at even shorter distances, we compared the slowness analysis measurements at 180 km with measurements at 60 km distance. Figure 2.5 gives examples for varying phase velocities at these two distances. The wave fields at these distances show quite different features in the slowness-depth domain but give consistent predictions for the wave field energy fluxes. Figure 2.6 compares the corresponding wave guide energy measured at 60 km and 180 km distances. Although a wide range of near-source structures and source depths are used to generate these measurements, they show very good linear relationships. This further verifies that we can use a small model to predict the energy distribution at greater distances.
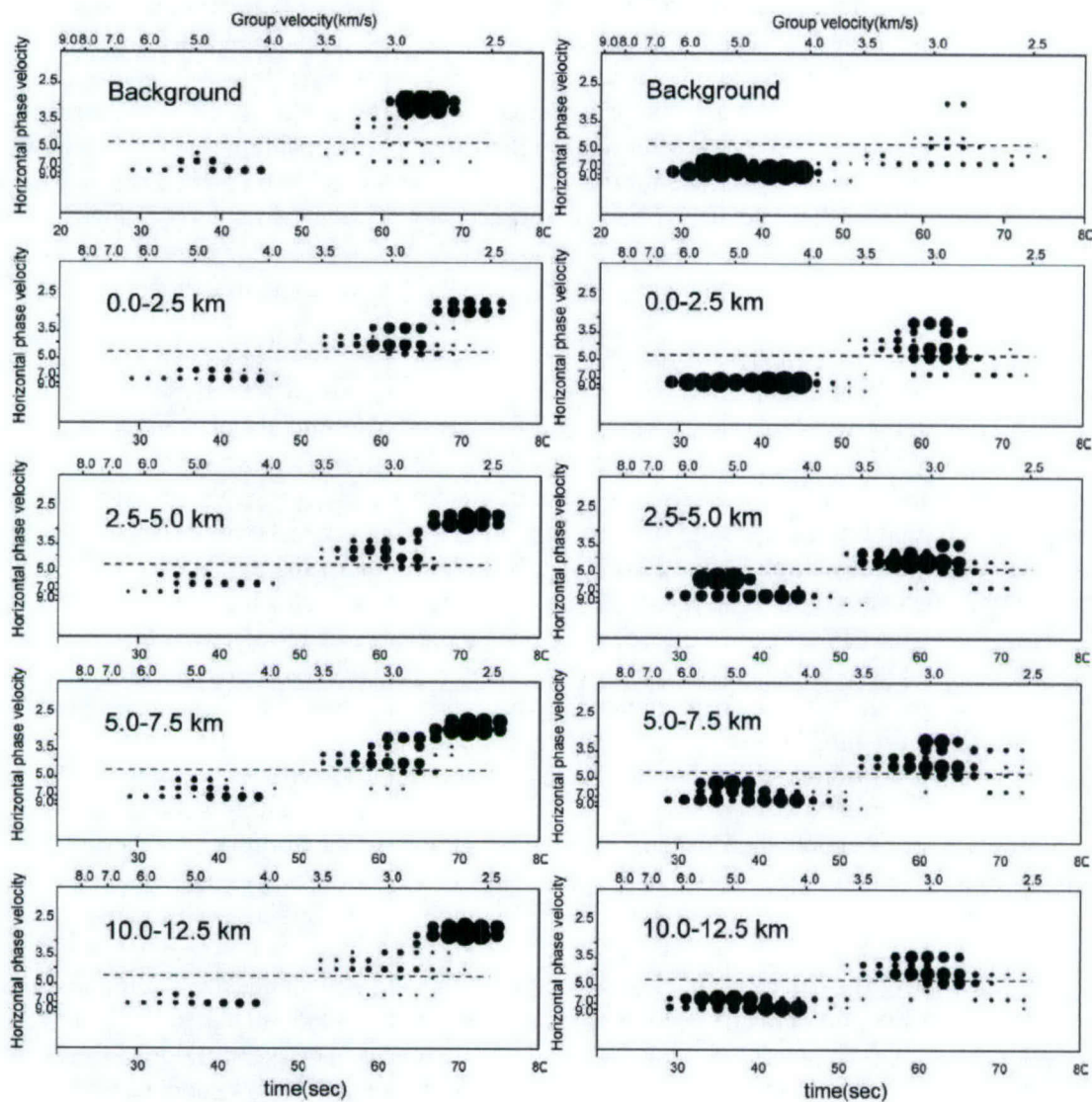
Figure 2.3. Slowness analysis for velocity models with random patches located at different depths. The left column is for the low-frequency band (0.3-1.5 Hz) and the right column is for the high-frequency band (2.0-5.0 Hz). The top panels show the background velocity model, and the rest of panels show random patches at different depths. For details, see the text.
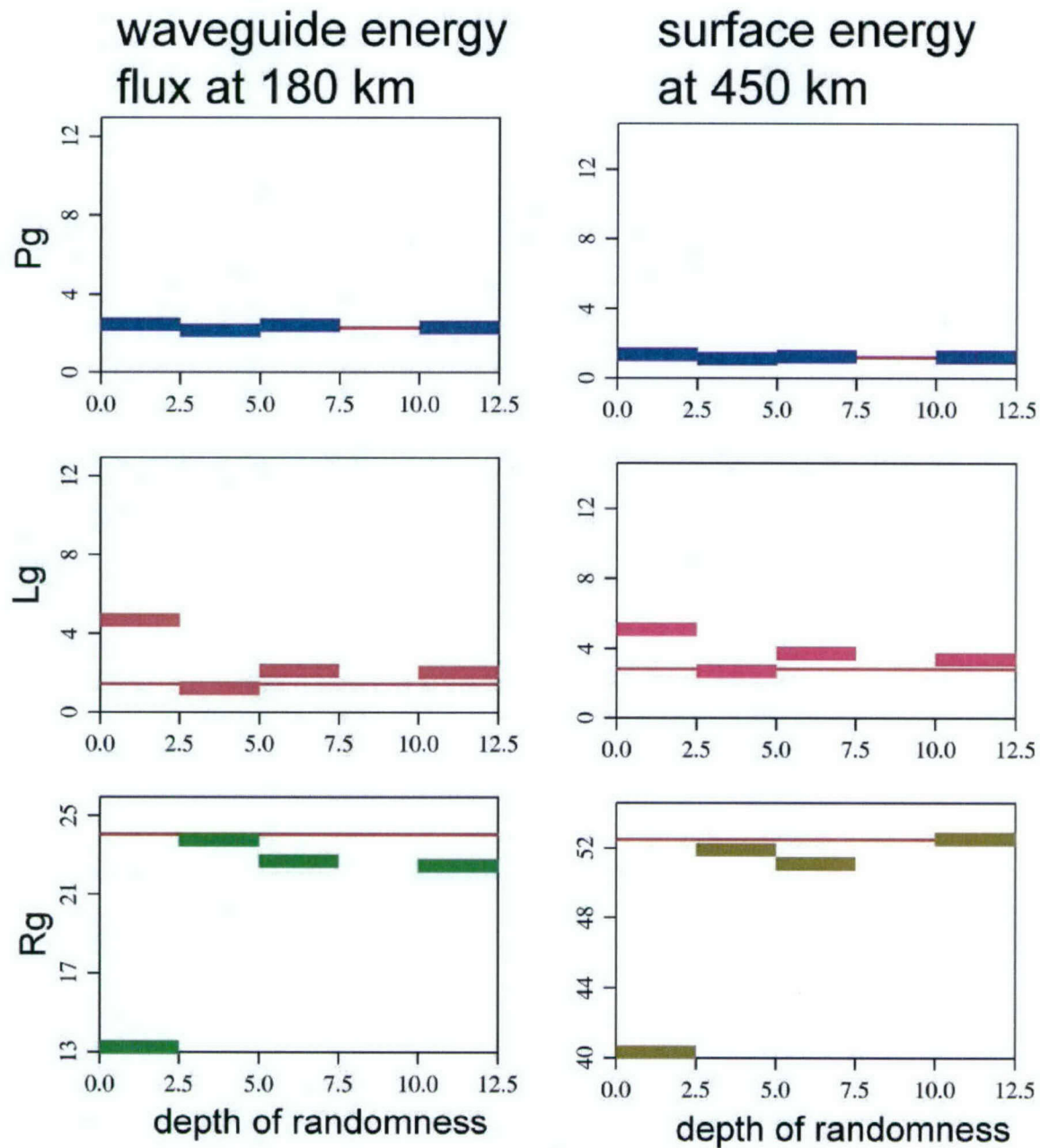
Figure 2.4. Comparison between waveguide energy flux at 180 km (left panel) and the wave energy on the surface at 450 km (right panel) for Pg, Lg and Rg windows. Different near source velocity models are used in the calculation. The frequency range is 0.3-1.2 Hz. Shown in each small panel is relative energy, the horizontal axis is the depth of the random patches, the vertical axis is the relative energy, thin line indicates the energy level for background model, short color bars indicate the energy changes due to the near source scatterings.

13
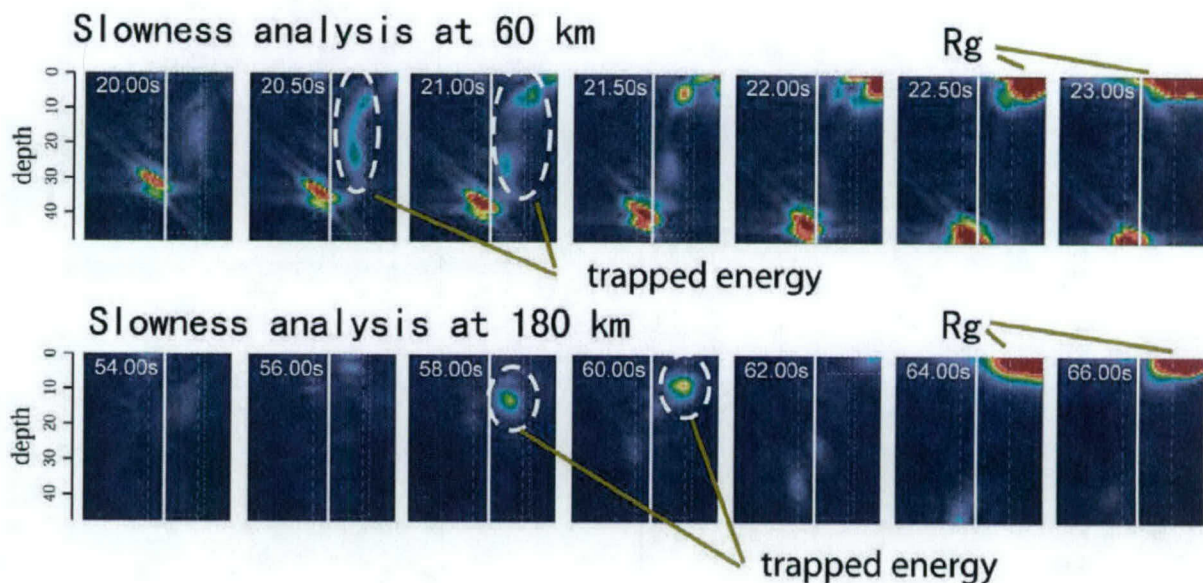
Figure 2.5. Examples showing the slowness analyses at distances of 60 km (upper panel) and 180 km (lower panel). The energy that can be trapped is indicated in the figure. The wavefields show quite different features at these distances but give consistent predictions for the trapped energy fluxes.
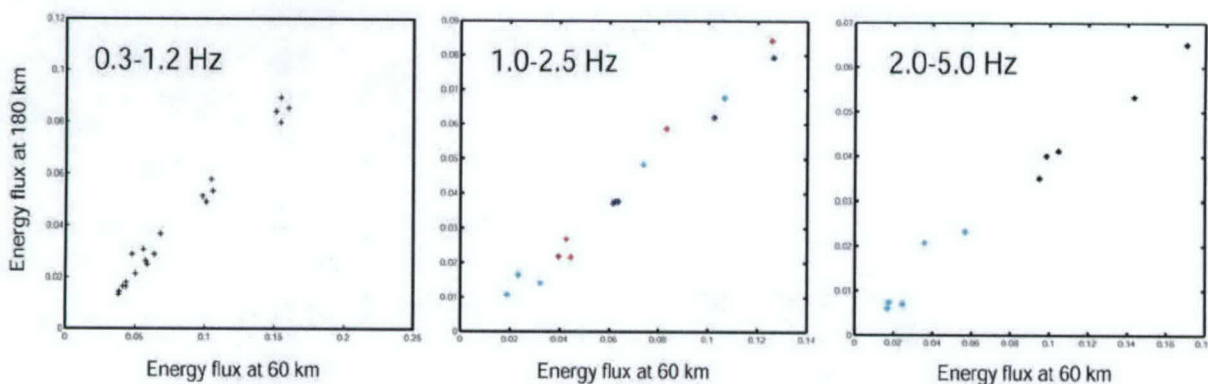
Figure 2.6. Comparison between trapped waveguide energy measured at 60 km (horizontal coordinate) and 180 km (vertical coordinate) for frequency bands 0.3-1.2 Hz, 1.0-2.5 Hz and 2.0-5.0 Hz. The results are from different velocity models and source depths. Different colors represent different velocity models. The results show a general linear relationship for all frequency bands.

14
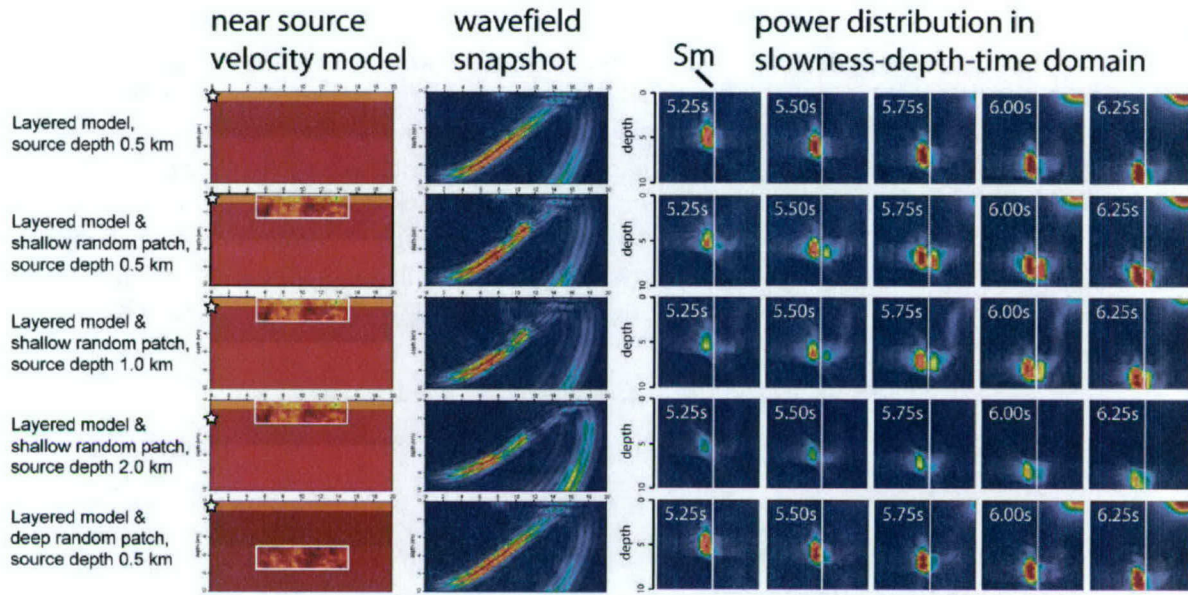
Figure 2.7. Summary of the P-pS-Lg wave coupling. From left to right are velocity models, wavefield snapshots and energy distributions in the slowness-depth domain. Details see the text.

2.4. Investigating the Regional Phase Excitation

2.4.1 The P-Lg and pS-Lg conversion

We first assess the importance of near-source lateral velocity variations that cause coupling between P, pS, and Lg. Figure 2.7 summarizes how the depth of heterogeneity affects the P-to-S coupling. From left to right are velocity models, wave field snapshots and energy distributions in the slowness domain. Slowness analysis is used at a distance of 16 km and depth 0-10 km. We use different source/model combinations in the simulations and test their effects on the P-to-S conversion. This example shows that without the lateral velocity heterogeneity, the energy of the free-surface reflected pS wave falls to the left of the upper mantle S-wave slowness and therefore cannot form trapped energy at regional distance. With a random velocity layer added to the model, the pS-wave front becomes distorted and its slowness content crosses the upper mantle S-slowness. Assessing the energy that builds to the right of the upper mantle S-slowness allows us to predict the Lg-wave component associated with P-to-S conversion. As can be seen from numerical examples, the depth of the source and the depth of the scattering region have strong effects on the P-to-S conversion and the partitioning of energy into trapped and leaking signals.

2.4.2 The Rg-to-Lg coupling

Rg-to-Lg coupling has long been proposed as a potential mechanism for low frequency Lg-wave excitation. However, there is disagreement as to whether this is a dominant mechanism or not. This is mainly due to the lack of knowledge about the actual mechanism of this process, for example, where this process happens, how much energy can be transferred from Rg to Lg, where the balance of the energy goes, and what is the frequency dependence of this process? Although

it is generally agreed that Rg-to-Lg coupling is caused by scattering in the near-surface environment, systematic investigation of this process is still lacking. Since the coupling process links the high end of the Rg band to the low end of the Lg band, the statistical feature of the lateral velocity or topography variation must play an important role in selecting the coupling. Any numerical test targeted to solve this problem must comprehensively take care of the excitation of the Rg (the source depth, shallow structure, CLVD component of the source), the frequency dependent scattering process (shallow structures or rough free surface with different statistical parameters) and sorting of the scattered energy to find the component eventually trapped in the waveguide as Lg energy. Using the FDSA method, we have conducted some numerical investigations of this problem.
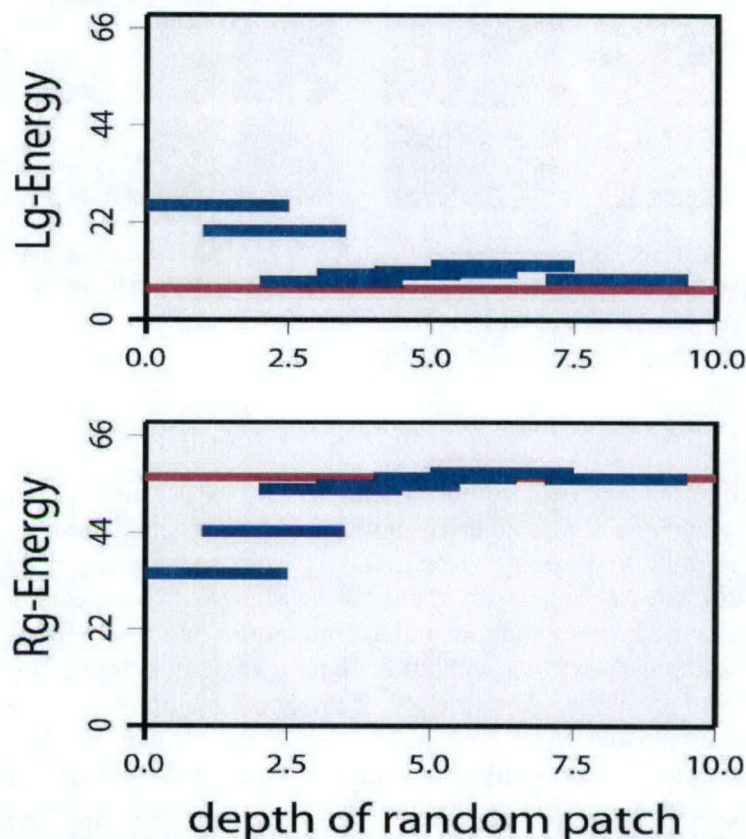
Figure 2.8. The apparent relationship between the Lg- and Rg-wave energy at 180 km in the waveguide vs. the depth of near source random patches. Frequency range is 0.3-1.2 Hz. Red dash lines are for the background layered model. Blue bars are for models with near source random patches at different depths.

We conducted two types of tests: a) for a shallow explosion source, we locate scattering regions at different depths; and b) for a shallow scattering region, sources are located at different depths. Figure 2.8 shows the waveguide energy fluxes for Lg and Rg versus the depth of near-source heterogeneities. The frequency range is 0.3-1.2 Hz, the overlapping domain for the two phases. Red lines are for the background model. Blue bars are for models with near-source random layers at different depths. For models with shallow scattering, Rg loses energy while Lg gains energy. Figure 2.9 gives the apparent relationship between the source depth and the Rg to Lg coupling. The three frequency bands are 0.3-1.5, 1.0-2.0 and 2.0-5.0 Hz, respectively. The

16

sources are located at different depths and scattering is provided by adding a near source random patch at the top of the crust. A shallower source raises both Rg and Lg energy while shallow scattering increases the Lg energy but decreases the Rg energy. This is consistent with some observations. The apparent Rg-Lg coupling occurs in the low frequency band and Pg-Lg coupling occurs in the high frequency band. Although these preliminary results provide an apparent relationship similar to some observations, they do not yet provide robust evidence that the energy lost from Rg is necessarily transferred to the Lg, since the S*-wave also has a similar excitation function, i.e., it favors shallow source and lower frequency excitation.
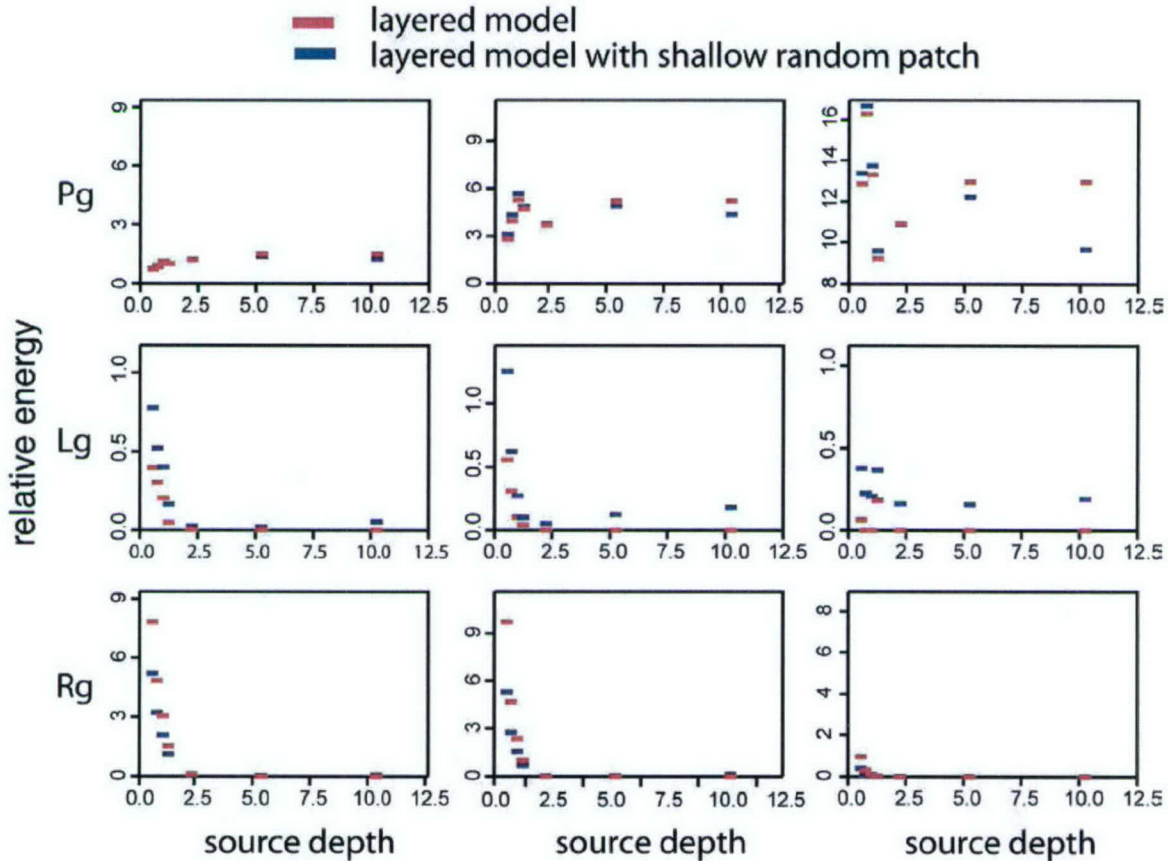
Figure 2.9. Effects of shallow near source scattering on the energy partitioning of Pg-, Lg- and Rg-waves. Sources are located at different depths between 0.5 and 10 km. Results for the background model are shown with red bars and results for models with random patches are shown with blue bars.

2.4.3 The S*-to-Lg excitation spectrum

For shallow spherical explosions, depending on the situation, the S*-wave may become a significant contributor to Lg (Gutowski, et al., 1984; Xie and Lay, 1994; Vogfjord, 1997). The amplitude of S* can be large as long as the source depth is within a fraction of a wave length from an interface. This makes its excitation highly dependent on the source depth and frequency. Figure 2.10 shows snapshots for explosion sources at 0.5 km and 3.0 km, respectively. This clearly shows that a shallow source generates larger S*- and Rg-waves. With the FDSA method, their energy can be easily investigated near the source region because of the distinct slowness for

17

these phases. Figure 2.11 gives slowness analysis at a 60 km distance for explosions at different depths. We can isolate and quantify the S* energy even within the complicated wavefield, which is very difficult to do with isolated surface synthetics. Using a band pass filter, the excitation function of the S*-wave can be obtained. This can be compared with various observations such as the spectral content of Sn and Lg, and will allow us to assess whether S* is in fact an effective Lg source relative to other mechanisms.
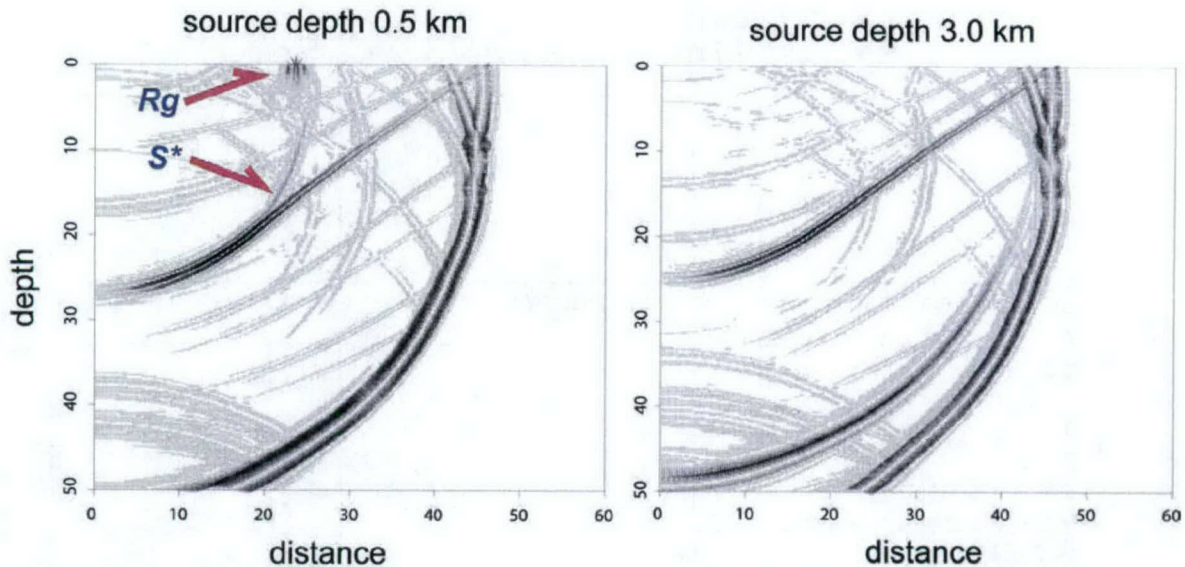
Figure 2.10. Wavefield snapshots for explosion sources at different depths. The source depths for left and right panels are 0.5 km and 3.0 km, respectively. A shallower explosion is a more efficient source for S* and Rg-waves.

We have shown some results that have intrinsic frequency dependence. These frequency variations are rooted in the underlying physical processes and are usually controlled by different characteristic scales. For example, the excitation of Lg by S*, Rg-to-S scattering and spall are all highly source depth dependent. The excitation spectra of specific phases depict the frequency dependence of these processes. Figure 2.12 gives the S*-to-Lg excitation spectra for sources in different models and at different depths. The result clearly shows that the excitation is generally favorable to lower frequency and shallow source depth. However, it is also model dependent. For a model with homogeneous upper crust (left panel), the distribution has a simple monotonous tendency. While for the EK model, which has an interface at depth 1.0 km (right panel), the excitation spectrum has a maximum at depth 1 km and a more complicated frequency dependency. This may result from the particular velocity model used. The frequency dependence of these excitation spectra can provide the basis for evaluating the dominant mechanisms for Lg-wave excitation, or for down-weighting particular mechanisms as being less significant. It will also provide the relationship between the observations and the characteristics of the source and near source structure.

18

Time-space-slowness windows used to pick S*-wave amplitude

Source depth = 0.5 km

| 20.50s | 20.75s | 21.00s | 21.25s | 21.50s | 21.75s | 22.00s |

Source depth = 1.0 km

| 20.50s | 20.75s | 21.00s | 21.25s | 21.50s | 21.75s | 22.00s |

Source depth = 2.0 km

| 20.50s | 20.75s | 21.00s | 21.25s | 21.50s | 21.75s | 22.00s |

Source depth = 3.0 km

| 20.50s | 20.75s | 21.00s | 21.25s | 21.50s | 21.75s | 22.00s |

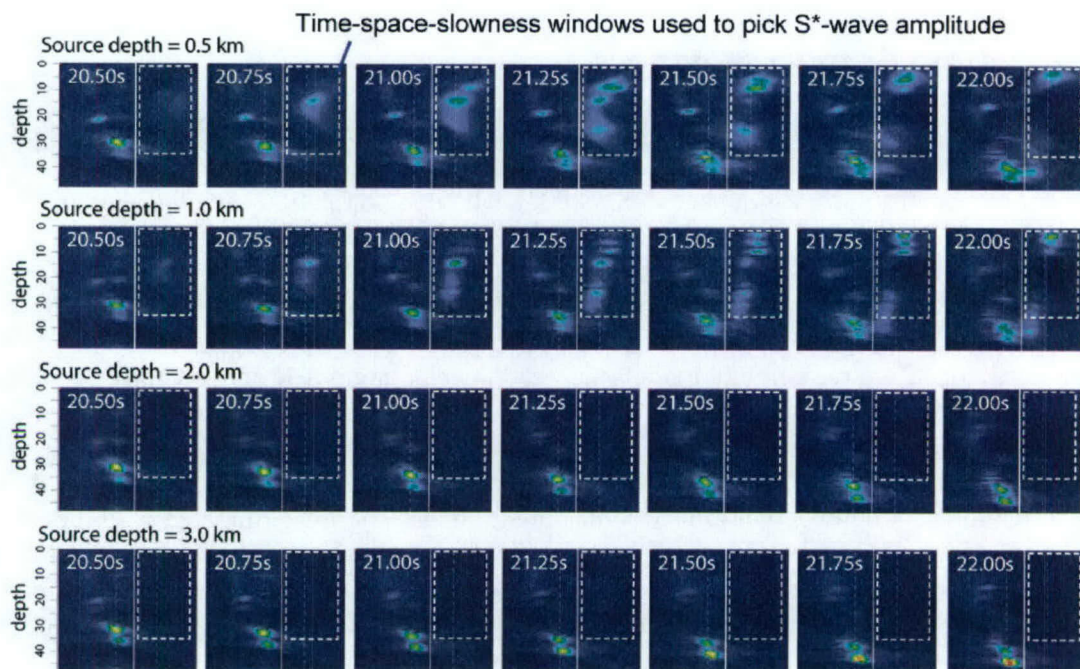Figure 2.11. Slowness analysis for investigating the S*-wave energy contributing to the Lg-wave. Different rows are for different source depths. Dash line rectangles indicate the time-space-slowness windows used to pick the S* energy.
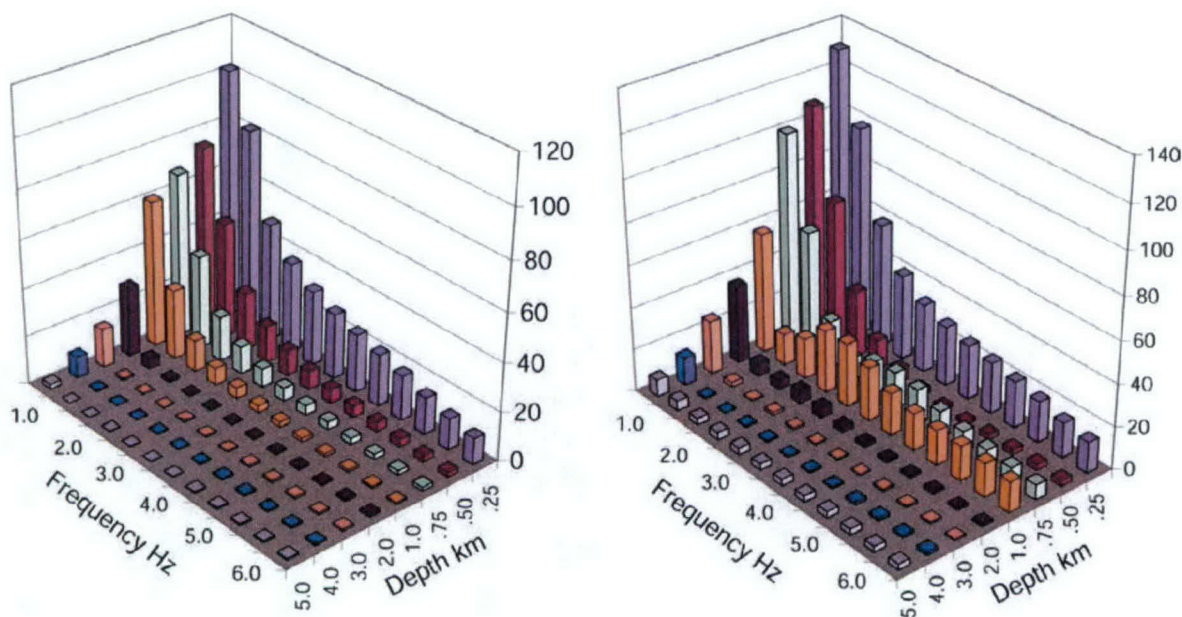

Figure 2.11. S*-to-Lg excitation spectra for sources at different depths. Left: a model with homogeneous upper crust, and Right: EK model. Details see the text.

19

2.4.4 The frequency dependent discriminants

Frequency dependent P/S ratios will depend on the excitation functions of multiple phases. Figure 2.12 shows observed Log (Pn/Lg) amplitude ratios in the frequency band between 0.5 and 10.0 Hz for explosions and earthquakes (Fisk 2003). The two populations exhibit poor separation below about 2 to 3 Hz and good separation at higher frequencies. Figure 2.13 gives a simulation of the Log(P/Lg) amplitude ratio in the frequency band 0.2 to 5.2 Hz. Two types of sources are used, an isotropic explosive source at 0.5 km depth representing a typical "explosion", and a 45 degree dip-slip dislocation source at 3.0 km depth representing a typical "shallow earthquake". Two velocity models are used in calculation, EK and EK plus a shallow near source random layer (depth 0-2.5 km, distance 5-25 km). The slowness analysis is conducted at a distance of 60 km. For the explosive source in the EK model, the Lg energy mainly comes from the S* phase. For the EK plus random layer model, it is expected that S*, P-to-Lg and Rg-to-Lg couplings will jointly contribute to the Lg energy. Compared with the explosive source, the somewhat deeper dislocation source is less affected by the shallow random layer. The result shows a general feature, which is similar to that from the observations (Figure 2.12). At the low frequency end, the earthquakes and explosions have similar P/Lg ratios but at higher frequencies, the explosive source generates less S energy.
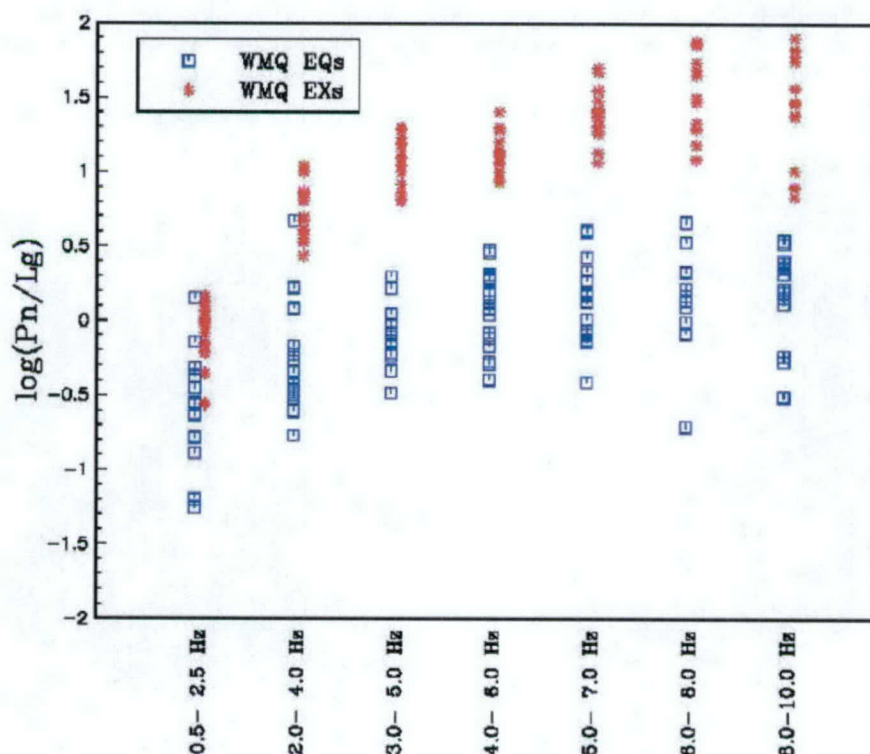
Figure 2.12. Log Pn/Lg amplitude ratios in frequency bands from 0.5 to 10.0 Hz for 20 Balapan nuclear explosions (asterisks) and 24 earthquakes (squares) recorded by WMQ (Fisk, 2003). The two populations exhibit poor separation below about 2 to 3 Hz and good separation at higher frequencies. SNRs for three of the nuclear explosions are marginal at frequencies above ~8 Hz

20

It is expected that with more complexities being added to the model (CLVD, different overburden structures and scattering models, source depth changes, different source time functions, etc.), these frequency dependent features will be complicated, but they can be systematically mapped out. This is the essential undertaking for placing regional phase energy partitioning on a sound physical basis. The numerical modeling will set up a link between the physical model and observable frequency dependent features, which can provide guidelines for improving the empirical discrimination relations. The feedback from the observations will guide the simulations towards the correct physical models as well.
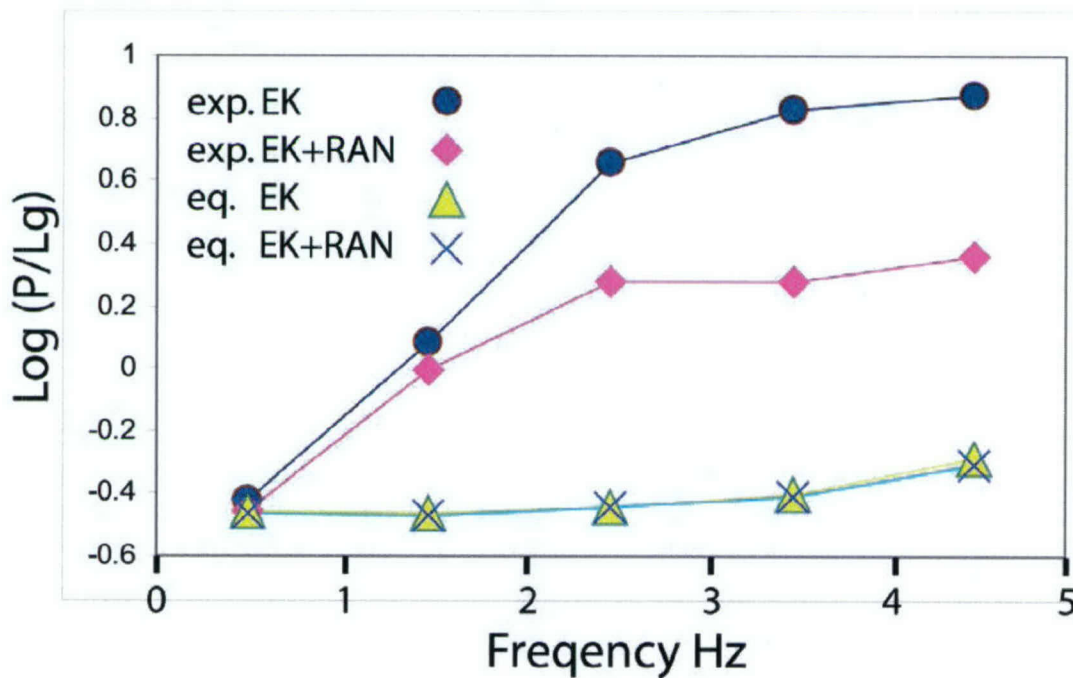
Figure 2.13. Simulated Log (P/Lg) amplitude ratios in frequency domain. The circle, diamond, triangle and cross represent explosion source in the EK model, explosion source in the EK model with shallow random patch, dislocation source in the EK model and dislocation source in the EK model with shallow random patch. The explosion source is located at depth 0.5 km and the dislocation source is located at depth 3.0 km.

3. THE PATH EFFECT ON LG WAVE PROPAGATION

3.1 Background

High-frequency regional wave propagation in complex crustal waveguides is one of the most challenging problems in theoretical and computational seismology. For the applications of regional waves to various geophysical problems, a good understanding of their propagation, scattering, attenuation and wave-type conversion, as well as the availability of tools to simulate and analyze these phenomena in complex crustal structures (including rough topography, Moho undulation and volumetric velocity heterogeneities of different scales) are crucial. Regional wave tomography for crustal structures, path correction for discrimination and yield estimation of low-yield nuclear tests, location determination of earthquakes or underground explosions using regional phases are examples of the possible applications. Monitoring the CTBT (Comprehensive Nuclear-Test-Ban Treaty) at regional distances is even more demanding of the simulation and analyzing tools. For this purpose, simulation algorithms are desirable for generating synthetic waveforms for high frequencies and propagation distances greater than 1000 km.

Substantial efforts have been made in modeling regional wave propagation. Methods based on layered earth models, such as the reflectivity and mode summation methods (e.g., Bouchon et al., 1985; Kennett, 1989, 1990; Maupin, 1989; Baumgardt, 1990; Campillo, 1990; Campillo and Paul, 1992; Campillo et al., 1993; Gibson et al., 1994) have very high efficiency and can be applied to relatively high frequencies, but they can be used only for very simplified cases with layered or smoothly varying layered models. Modeling techniques that can treat realistic 3D heterogeneous media rather than smoothly varying layered media are needed to test and study many observations and hypotheses. Sudden changes of crustal thickness, strong lateral variations and irregular 3D heterogeneities are among the problems requiring new modeling methods. As pointed out by Campillo et al. (1993), actual Lg amplitudes were reduced more than 10 times for paths passing through an anomalous zone on the east side of the Alpine range, while the modeling results using existing methods (including the effect of known large-scale lateral structural variation) only account for 20 - 30 % of the amplitude reduction. Other mechanisms such as scattering and attenuation by small-scale heterogeneities must be taken into account.

Kennett (1984, 1998), Maupin and Kennett (1987) developed a coupled mode method for calculating guided seismic waves in horizontally varying structures. The method works well for relatively low frequency waves in moderately heterogeneous models. However, the implementation of the method for high frequency 3-D models still requires formidable computational efforts.

Cormier and Anderson (1996, 1997) applied elastic Born scattering (in the regime of Rayleigh scattering) to the locked-mode solution for plane layered media to calculate the effects of small-scale heterogeneities. However, the approximation is limited to single scattering and is only good for heterogeneities with scales much smaller than the wavelength. Ray methods have very limited success in modeling regional waves due to the chaotic behavior of rays caused by the multiple reflections of the free-surface and Moho. Keers et al. (1996a, b) applied the Maslov integral method to avoid the caustics and pseudo-caustics (caustics of plane waves) by working

in the phase-space. However, when chaos develops in the ray system, there are more complicated caustics for which the Maslov method does not work. In addition, ray-tracing computation is very time-consuming in this case. An alternative and flexible approach using ray-tracing has been developed by Kennett (1986), Bostock and Kennett (1990) and Kennett et al. (1990), in which ray diagrams are used to study Lg waves when crossing structural boundaries. The method agrees well with modal calculations and can be applied to surface topography, 3-D crustal structures and other cases. However, the method cannot provide information on wave phenomena for complicated waveguides.

Finite-difference methods are general numerical methods and have been extensively applied to regional wave propagations (e.g., Xie and Lay, 1994; App et al., 1996; Goldstein et al., 1996, 1997, 1999; Husebye and Ruud, 1996; Jih, 1996; Nolte et al., 1996; Jones et al., 1997; McLaughlin and Wilkins, 1997; Bradley and Jones, 1998, 1999) and pseudo-spectral methods (e.g., Kosloff et al., 1990; Orrey et al., 2003; Archambeau et al., 1996; Schatzman, 1996; Furumura and Kennett, 1997). Theoretically the method can deal with arbitrarily heterogeneous media. However, it is necessary to use very dense spatial sampling to avoid grid dispersion for long distance regional wave propagation. The capability of the present day computers usually restricts them to short propagation ranges and relatively low frequencies, which prevents them from being applied to more realistic cases.

The state of the art of the traditional simulation techniques for regional waves has its application to relatively low frequencies and short propagation distances. Correspondingly, the volume heterogeneities and surface irregularity in the crustal models are limited to rather large scales. However, high frequency regional waves up to 20 Hz and higher have been observed over distances ranging from a few hundred kilometers to more than one thousand kilometers (e.g., Ni et al, 1996; Herman et al., 1997; Lay et al., 1999). Since high-frequency waves can be used for event locations with high accuracy, simulation and modeling of high-frequency regional wave propagation are very desirable for many applications. For high frequency wave propagation, scattering and attenuation, the role of small-scale heterogeneities and surface roughness is important.

The existence of small-scale heterogeneities in the crust and the associated seismic wave scattering has long been known among seismologists (e.g., Aki, 1980; Wu and Aki, 1988, 1989, 1990; Sato and Fehler, 1998). However, the effects of these heterogeneities on guided wave (L_g) propagation in the crust have not been seriously explored. The reasons may be the following. First, the spectra, strength and distribution of the small-scale heterogeneities in different regions are not clear. Very few data sets can be used to characterize the paths concerned. Second, there is a lack of analytical and numerical tools to model or analyze their influence on the guided wave propagation. The theory of wave propagation in unbounded random media has been well developed. However, for waves in complex crustal waveguides with random heterogeneities, the theoretical difficulties are overwhelming, and no analytical tool is available for performing realistic calculations. Therefore, numerical methods for simulating regional wave propagation in complex waveguides with small-scale heterogeneities are highly desirable. It has become clear that small-scale heterogeneities are widely distributed in tectonically active regions. Strong topographic variation is the manifestation of tectonically active regions and often the indication of small-scale heterogeneities. Figure 3.1 gives a topographic profile (top panel) and its power

spectrum (bottom panel) for a path crossing Tibet Plateau. The slope of the spectral roll-off is close to $1/k$, a flicker noise spectrum, very rich in small-scale variations. This spectrum is similar to the observations of the sonic well-log in the KTB super-deep continental drilling well (Wu et al., 1994; Jones and Holliger, 1997; Goff and Holliger, 2002). The spectra there have also a $1/k$ slope. Recently, Goff and Holliger (2002) explained the $1/k$ spectra as a combination of hierarchical, multi-scale heterogeneities. Overall, the $1/k$ spectra demonstrate richness of small-scale heterogeneities.
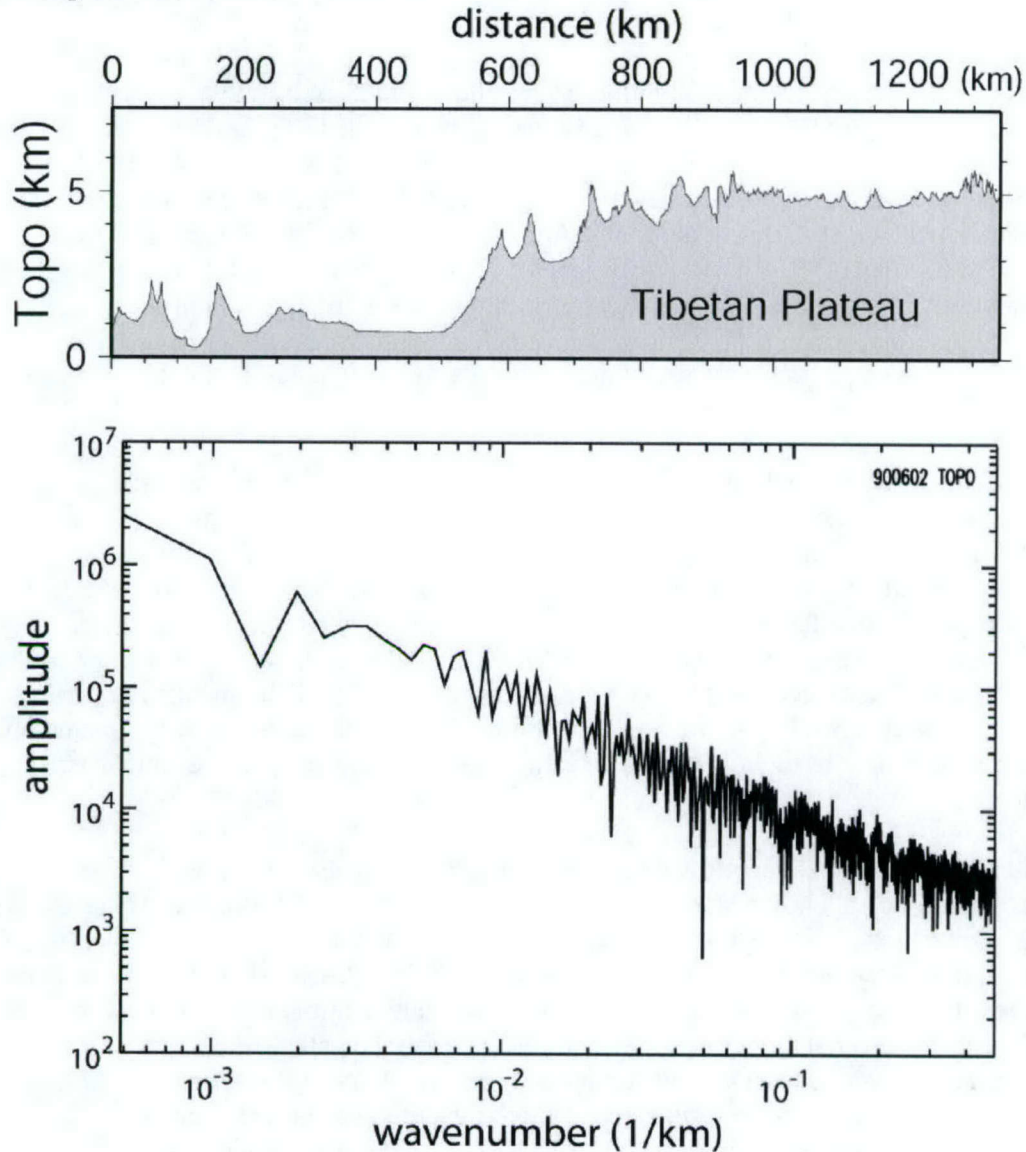

Figure 3.1 The topographic profile and its power spectrum for a path crossing the Tibetan Plateau.

Recently, the generalized screen method has been introduced into seismic wave simulations and applied to the problems of both exploration and theoretical seismology. The generalized screen method is based on the one-way wave equation and the one-return approximation. The one-way

generalized screen propagator (GSP) neglects backscattered waves, but correctly handles all the forward multiple-scattering effects, e.g., focusing/defocusing, diffraction, interference, and conversion between different wave types. The one-return approximation is also called the De Wolf approximation (De Wolf, 1971, 1985), which neglects the reverberation between screens and can simulate multiple-forescattering-single-backscattering (MFSB). Significant progress has been made on the development of an elastic complex screen (ECS) method for modeling elastic wave propagation and scattering in arbitrarily complicated structures (Wu, 1994, 1996; Xie and Wu, 1995; Wild and Hudson, 1998; Wu and Wu, 2001). The method is two to three orders of magnitude faster than the elastic finite-difference method for medium size 3D problems. The screen method has been successfully used in forward modeling (Wu, 1994; Wu and Huang, 1995; Xie and Wu 1995, 1996, 1999, 2001; Wu and Wu, 2001) and as backpropagators for seismic wave imaging/migration in both acoustic and elastic media (e.g., Wu and Xie 1994; Huang and Wu 1996; Xie and Wu, 1998, 2004; Huang et al., 1999a,b; Jin and Wu, 1999; Jin et al., 1999).
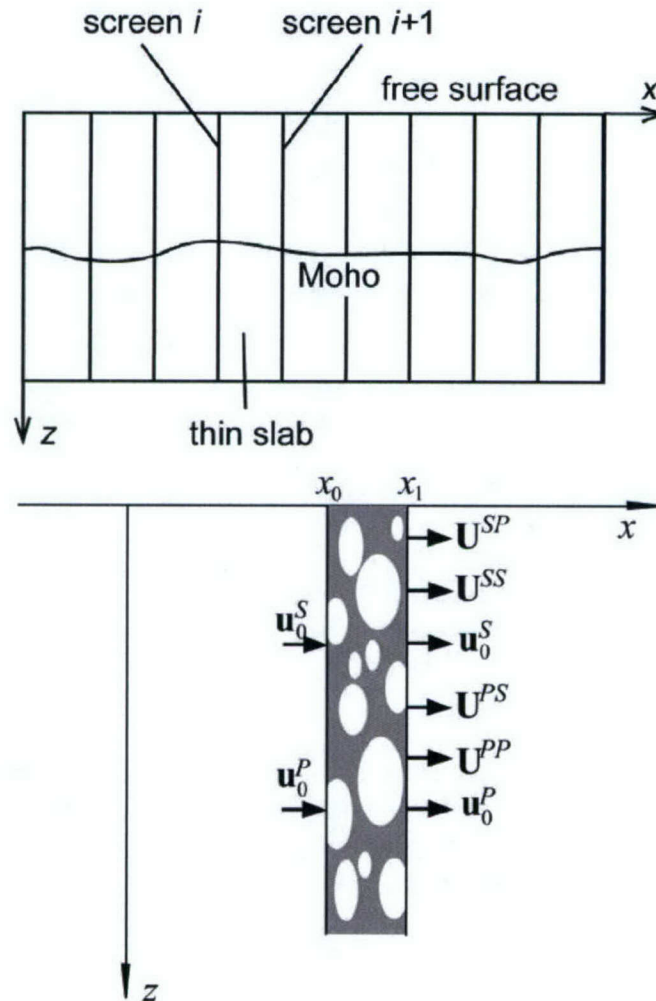

Figure 3.2 (A) Upper panel: geometry using the screen method to simulate Lg wave, and (B) lower panel: sketch showing the interaction between the incident waves and the thin slab.

3.2 The Generalized Screen Propagator for Guided Waves

In the crustal waveguide environment, major wave energy is carried by forward propagating waves bouncing up and down between the free surface and major geophysical discontinuities such as the Moho and Conrad discontinuities. Beyond the critical angle, these waves are systematically dominated by small angle waves trapped in the crustal waveguides. Therefore, the neglect of backscattered waves in the propagation will not distort the main features of regional waves in most cases. With this approximation, the method becomes a forward marching algorithm in which the next step of propagation depends only on the present values of the wavefield in a transverse cross-section and the heterogeneities between the two cross-sections. To formulate the problem, we divide the crustal wave guide into a sequence of vertical slabs. The horizontal direction is chosen as the main propagation direction. The geometry of the model is shown in Figure 3.2a. Choosing one slab as the example, Figure 3.2b shows the interaction between the incident waves and the thin slab. By introducing the local Born approximation, both wavefields and the elastic parameters can be separated into two parts, the background values and the perturbations. The incident P- and S-waves $\mathbf{u}_0^P$ and $\mathbf{u}_0^S$ enter the slab from the vertical plane at x_0. After the incident waves pass through the thin slab between x_0 and x_1, interacting with the heterogeneities within it, there will be both incident waves and different types of forward scattered waves at the exit plane at x_1. The new P-wave $\mathbf{u}^P = \mathbf{u}_0^P + \mathbf{U}^{PP} + \mathbf{U}^{SP}$ is composed of incident P-wave and scattered P-waves from incident P- and S-waves, and the new S-wave $\mathbf{u}^S = \mathbf{u}_0^S + \mathbf{U}^{PS} + \mathbf{U}^{SS}$ is composed of incident S-wave and scattered S-waves from incident P- and S-waves. The propagation can be solved using perturbation theory. The interaction between the incoming wave and a heterogeneous slab can be completed with two separated steps. The interactions between the incoming waves and the perturbations are conducted in the spatial domain which give the coupling between different wave types. Plane wave propagation through the background medium is conducted in the wavenumber domain. In both domains, the calculations are local and highly efficient. There is no time-consuming spatial or wavenumber domain convolution involved. The forward and inverse fast Fourier transforms alternate the wavefield between the two domains. By iteratively using this process and making the output from one thin slab the input of the next thin slab, the wavefield can be propagated prograssively through the entire model.

The conventional wavenumber integral method is for horizontally layered model and the integral is along horizontal wavenumber k_x. On the contrary, the elastic screen method for propagating guided waves in crustal environment prefers the horizontal as the main propagation direction. Under this geometry, the postcritical reflections result in small-angle dominance in wave propagation and scattering, which is necessary for methods based on a small angle approximation. Our velocity model is composed of vertical slabs and the integral is along vertical wavenumber k_z. Wavenumber integration has to be modified for the vertical screen geometry.
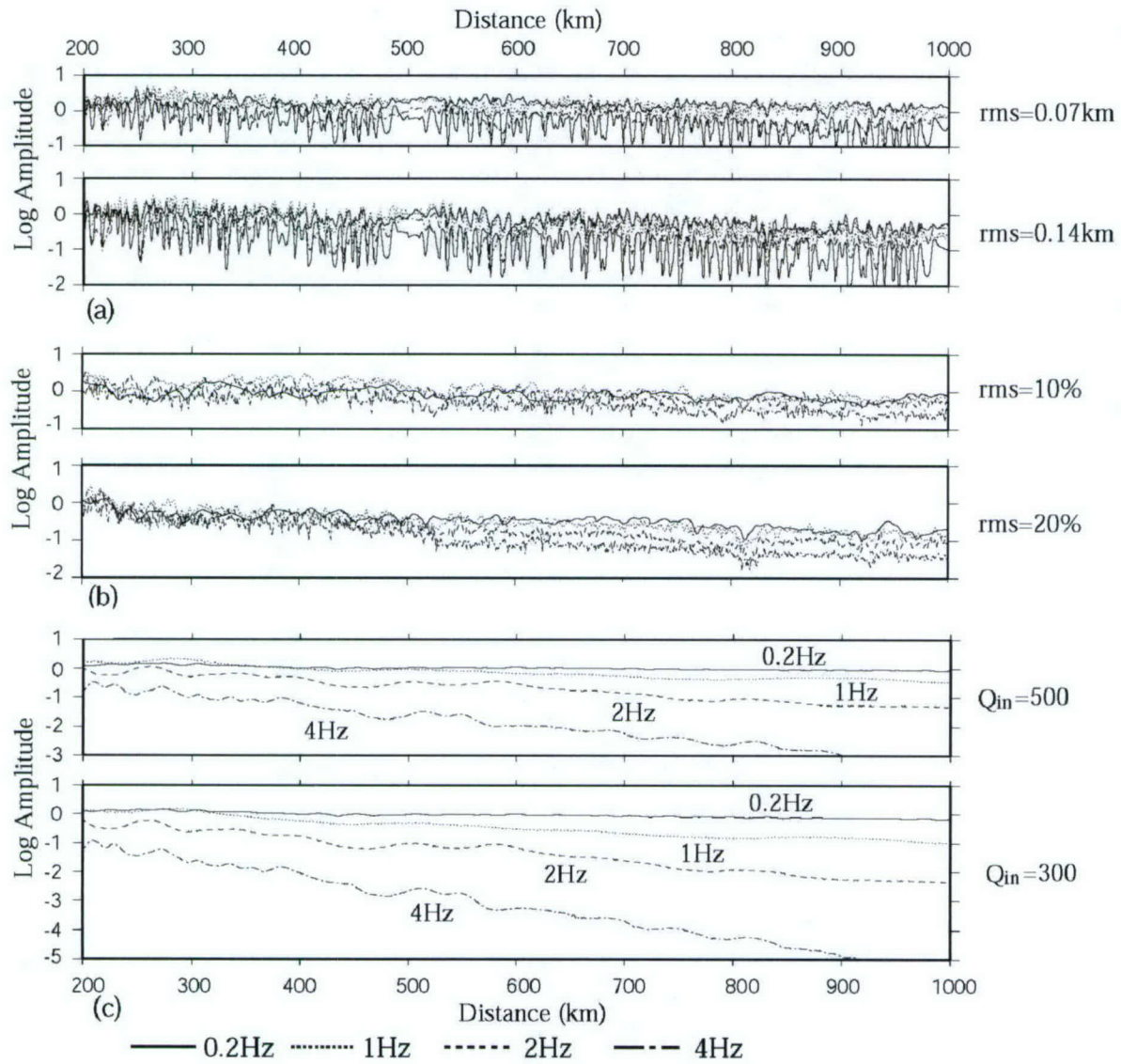
Figure 3.3 **Lg spectral amplitudes at four different frequencies versus distance for crustal models with topographies only (a), crustal heterogeneities only (b), and intrinsic attenuation only (c). Topography with rms=0.07km has a fluctuation of 0.87~0.75km in height. Q_{in} denotes quality factor of shear wave.**

GSP is accurate for small-angle propagation and scattering (near horizontal for crustal wave guide environment). A half-space screen propagator has been introduced by Wu et al. (1996, 2000) to accommodate the free-surface boundary condition and treat the SH-wave propagation in complex crustal waveguides. The new one-way method for modeling regional SH-waves has

27

been calibrated extensively with various full-wave methods for different crustal models, such as the wavenumber integration method for flat structures and finite-difference method for heterogeneous crustal waveguides. Excellent agreements with these methods demonstrated the validity and accuracy of the new one-way method. For a model with propagation distance of 250 km, dominant frequency at 0.5 Hz and with similar accuracy, the GSP method is about 300 times faster than the finite-difference method. The method has been applied to the simulation of Lg propagation in random media and the related energy partition and attenuation (Wu et al., 2000). It is found that the leakage attenuation of Lg waves caused by forward large-angle scattering from random heterogeneities, which scatters the guided waves out of the trapped modes and into the mantle, may contribute significantly to Lg attenuation and blockage in some regions. The apparent Q for leakage attenuation as a function of normalized scale length (ka) of the random heterogeneities agrees well with the scattering theory. Later the SH screen propagator was extended to the case of irregular surface topography by conformal or non-conformal topographic transforms (Wu et al., 1999; Wu and Wu, 2001). In the conformal transform method, the coordinate system is rotated according to the local topographic slope, and the mirror image method can be applied to the local plane surface; the non-conformal method is a surface flattening transform which turns the free surface topography into modified volume perturbations of elastic parameters. The former method is suitable to deal with smoothly varying topography; while the non-conformal method can treat rough but moderate topography.

In the case of P-SV elastic screen propagators, the derivation and application of one-way screen propagators are much more complicated. Unlike for SH-waves, the image method of generating the half-space Green's function cannot be used to account for the effect of free surface. Plane wave reflection calculations are incorporated into the elastic screen method (Wu et al., 2000). Body waves including the reflected and converted waves can be calculated by real wavenumber integration; while surface waves (Rayleigh waves) can be done with imaginary wavenumber integration.

3.3 Simulation of Lg Wave Propagation and Blockage Using Screen Method

Observations frequently show that regional Lg phase attenuation is related to many factors such as laterally heterogeneous velocity structure, changes in crustal discontinuities, crustal thickness, topographic features, anelastic attenuation, etc. However, the mechanism of Lg wave attenuation has not been fully understood, especially for tectonically active regions that have abnormally low Lg Q. For example in the eastern Tibetan Plateau 1 Hz Lg Q is about 126 (Xie, 2002); and it is about 200 – 267 in various regions of the western United States (Xie, 1998), prior numerical simulations tend to under estimate Lg attenuation or blockage. This can be attributed to two reasons. On one hand, realistic crustal models are quite complex so that the parameterized models could be poor approximations. On the other hand, the existing simulation approaches may not have the capacity to handle the effects of the various factors mentioned above.

In this section, using the screen method incorporated with anelastic quality factor Q_{in}, Lg wave simulations, including the effects of random topographies, crustal heterogeneities and anelastic attenuation are conduced separately. We estimate apparent Lg Q and its power-law frequency dependence associated with different attenuation mechanisms. Then, we synthesize Lg wave responses to a real crustal geometry in the Tibetan Plateau, assuming different heterogeneities

and intrinsic attenuations. Preliminary simulation results reveal high Lg attenuation or blockage after introducing low Q_{in} (intrinsic quality factor of shear wave) into the model.
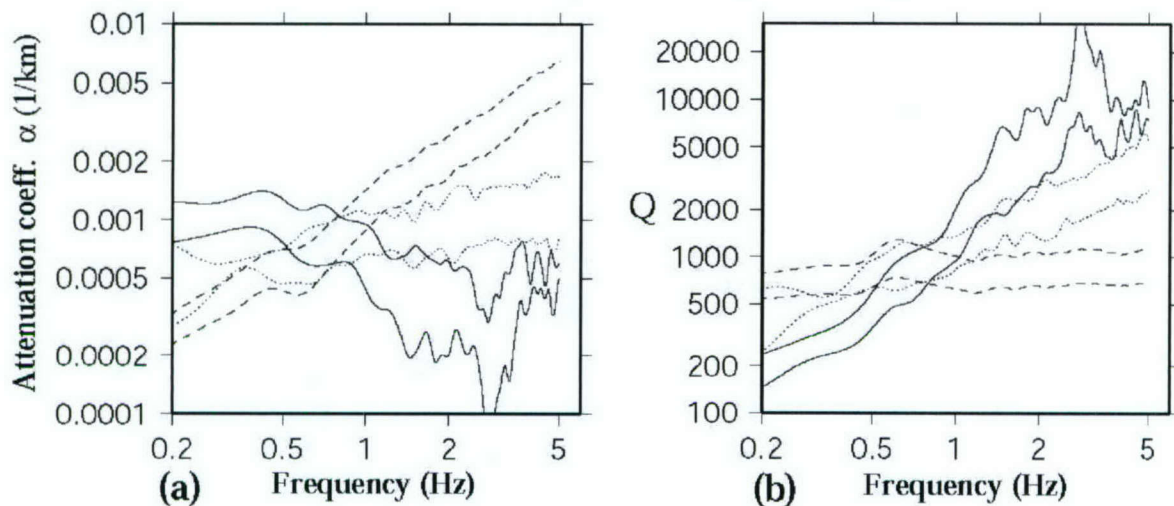

Figure 3.4 (a) Attenuation coefficient versus frequency, (b) Apparent Lg Q versus frequency. Solid lines correspond to the models with random topographies, dotted lines to models with volume heterogeneities, and dashed lines to the anelastic crustal waveguides.

3.3.1 Surface and volume scattering, anelasticity and Lg Q

The crustal model for simulations consists of a crustal layer and a half-space mantle. The parameters of the crust and mantle are $V_{crust} = 3.5km/s$, $\rho_{crust} = 2.8g/cm^3$, $V_{mantle} = 4.5km/s$, and $\rho_{mantle} = 3.1g/cm^3$. The thickness of the crust is 32 km. Two random models are used for the free surface topography. Both of them have the same correlation length of 2.5 km but have different RMS fluctuations. The first has a RMS of 0.07 km (elevation between -0.75 and 0.87 km) and the second has a RMS of 0.14 km (elevation between -1.5 and 1.75 km). Random models with exponential correlation function are used for crust volume heterogeneity. The correlation lengths are 10 km in range and 5 km in depth. The RMS values used are 10% and 20%, respectively. A source is located at a depth of 8 km and has a spectrum function given by:

$$S(f) = \frac{1}{1 + (f/f_c)^2}$$

where f is frequency and $f_c = 2Hz$ is the dominant frequency. For the screen method, the step length for each forward propagation is 125 m. The depth sampling interval is 250 m. The number of samples in depth is 512. The number of screens is 8000 corresponding to a regional distance of 1000km. We calculated 6 sets of Lg synthetic seismograms for different crustal models. Figure 3.3 shows spectral amplitudes versus distance for four different frequencies: 0.2, 1., 2., and 4 Hz. Figure 3.3a involves the scattering effect of irregular surface only. Fluctuation of Lg spectral amplitudes versus distance increases as frequency and/or the roughness of the topography increase, while the average spectral amplitudes show a weak attenuation for either low or high frequencies. Figure 3.3b involves the scattering effect of volume heterogeneities only. Fluctuation of Lg spectral amplitudes is weak compared to the effect of rough topography. Figures 3.3a and 3.3b show that although rough topography and volume heterogeneity may

directly affect the Lg wave behavior, they cannot fully account for high Lg attenuation or blockage. Figure 3.3c involves only the effect of anelastic attenuation. We see that Lg spectral amplitudes vary smoothly with distance, and high-frequency Lg waves show strong attenuation.

Table 3.1 Estimated Q_0 and η

	Topography		Heterogeneity		Intrinsic Q_{in}	
	D=0.07km	D=0.14km	B=10%	B=20%	500	300
Q_0	2029	945	1345	827	508	313
η	2.320	1.700	0.888	0.73	0.057	0.056

Note: D denotes the RMS for random topography and B denotes the RMS for random volume heterogeneity.

Under 2D model, assume that Lg spectral amplitude can be expressed as

$$A_{Lg}(f) = S(f)e^{-\frac{\pi f x}{Q v}} = s(f)e^{-\alpha x}$$

where α is the attenuation coefficient, x the propagation distance, v the Lg group velocity, and Q is the frequency-dependent apparent Lg Q. Then we can calculate attenuation coefficient and Lg Q by linearly fitting Lg spectral amplitudes shown in Figure 3.3. Figure 3.4 shows the estimated attenuation coefficients and the frequency dependence of the apparent Lg Q. Solid lines correspond to the models with random topographies, dotted lines to the models with volume heterogeneities, and dashed lines to anelastic crustal waveguides. For different attenuation mechanisms, apparent Lg Qs show different frequency-dependency.

The observed Lg Q usually fits a power-law frequency dependence as:

$$Q_{Lg}(f) = Q_0 f^\eta$$

where Q_0 is the Lg Q at 1 Hz reference frequency and η is the power-law frequency dependence. Using the above relationship and Figure 3.4b, we can estimate Q_0 and η (listed in Table 1). Table 3.1 shows that the simulated Lg frequency dependence η for homogeneous anelastic crusts is much smaller than the observations from earthquakes and explosions ($0.3 < \eta < 0.6$), while the η associated with scattering by random topographies or volume heterogeneities varies strongly. It is possible to generate appropriate η by mixing the contributions from both intrinsic and scattering attenuation under the constraint of matching real data.

3.3.2 Lg wave simulation with real crustal waveguides

Although the propagation of Lg has been observed across most of Asia, it has not been observed for paths crossing the Tibetan Plateau. It has been demonstrated that the Lg wave undergoes abnormally strong attenuation in these regions. Figure 3.5a shows an actual crustal cross-section in the Tibetan Plateau (Fan and Lay, 1998). This cross-section has severe changes in surface topography and lateral velocity structure. We will introduce heterogeneity and intrinsic attenuation into the crustal model to investigate the mechanism of Lg attenuation and blockage. Topography data has a resolution of 1 km in range and Moho depth data has a resolution of 10 km in range. For purpose of numerical simulation using the screen method, both data sets are

linearly interpolated up to a sampling interval of 0.125 km. The rest of the parameters are the same as used in Figure 3.3. The SH synthetic seismograms are calculated for regional distances up to 1000 km and the Lg wave energy is obtained by summing up the energy from all frequency components. Figure 3.5b shows Lg wave energy versus distance for models with different heterogeneities and intrinsic attenuations. The four lines from top to bottom correspond to: (1) A perfect elastic homogeneous waveguide; (2) A perfect elastic model with 10% RMS volume heterogeneity; (3) A crustal model with 10% RMS volume heterogeneity plus an intrinsic Q of 500; and (4) A crustal model with 10% RMS volume heterogeneity plus an intrinsic Q of 300. We see that for a perfect elastic waveguide, Lg energy fluctuation closely follows the topography and Lg energy decay is generally weak. Up to the distance of 1000 km high-frequency Lg phase is still rather strong. After introducing intrinsic attenuation, Lg waves show higher attenuation.
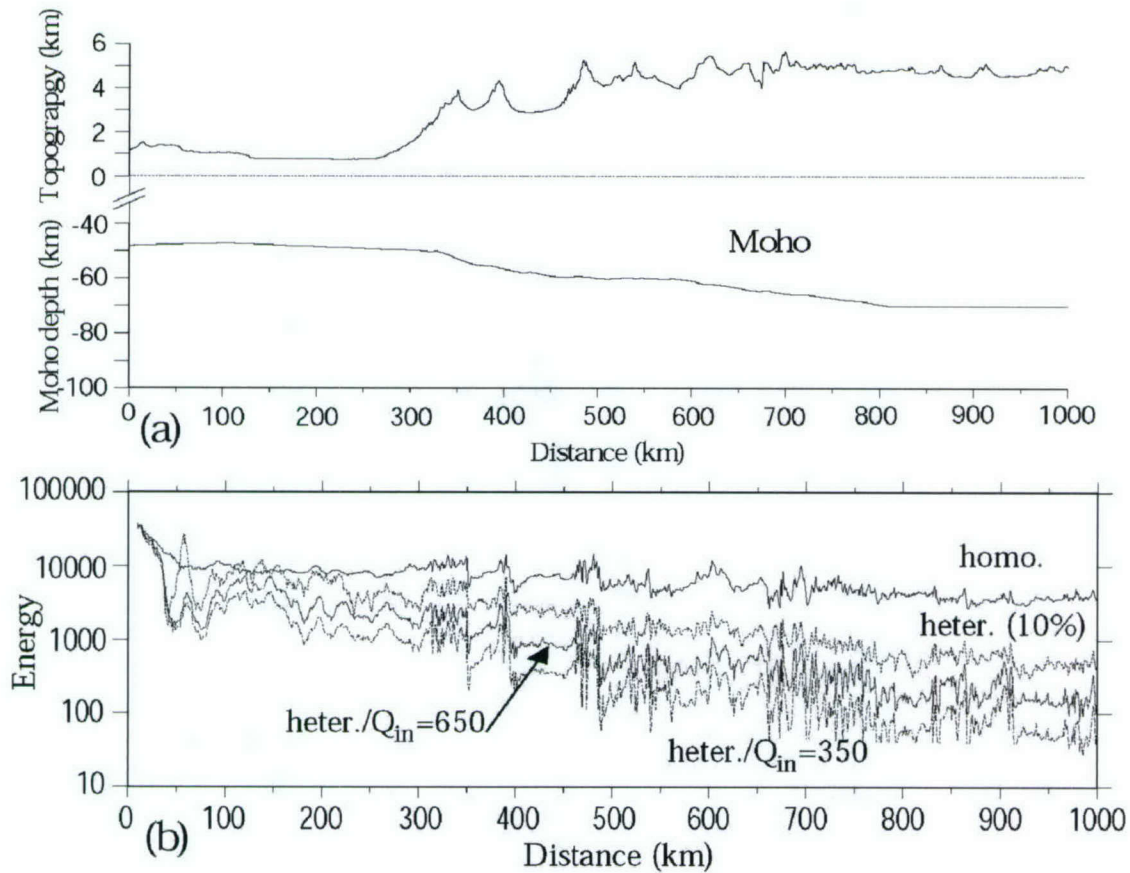
Figure 3.5 (a) A cross-section in Tibetan Plateau (Fan and Lay, 1998). (b) Lg wave energy versus distance for crust models with different small scale heterogeneities and intrinsic attenuations, where solid line is for homogeneous elastic waveguide; dashed line is for crust with 10% RMS heterogeneity, dotted and dotted-dashed lines are for crust models with different intrinsic attenuations (Q_{in} = 500 and 300) plus 10% RMS heterogeneity.
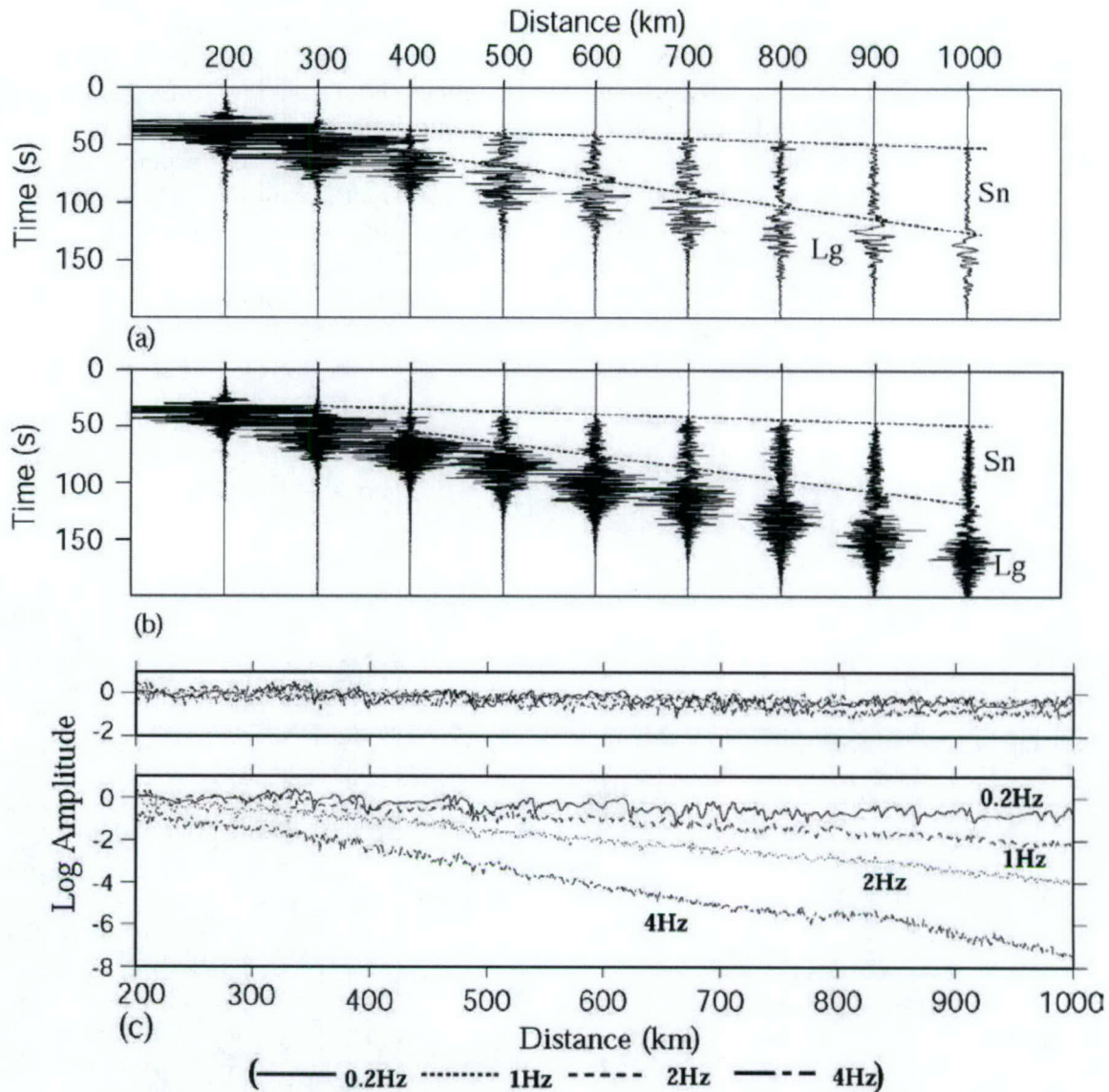
Figure 3.6 (a) Synthetic seismograms for the crust with variable anelastic attenuation along the path, (b) synthetic seismograms for the elastic crust with rms=10% heterogeneities, and (c) Lg spectral amplitudes versus distance at 4 different frequencies calculated from (a) and (b), respectively.

In the next example, we use a model with variable intrinsic attenuation along the propagation path. We assign the Q_{in} to be 450 for distances less than 300 km; 250 for distances between 300 and 800 km; and 125 for distances greater than 800 km. Corresponding synthetic seismograms are shown in Figure 3.6a. The time axis is reduced by a velocity of 6 km/s. We see that high-frequency Lg waves are weak at 800 km and absent at 1000 km. For comparison, synthetic seismograms for a perfect elastic heterogeneous waveguide are given in Figure 3.6b. High-frequency Lg waves are still strong at distances up to 1000 km. Figure 3.6c shows Lg spectral amplitudes at four different frequencies versus distance calculated from synthetic seismograms in Figures 3.6a and b. The variable slope of the high-frequency Lg spectral amplitudes at different distances results from the variable intrinsic Q along the propagation path.
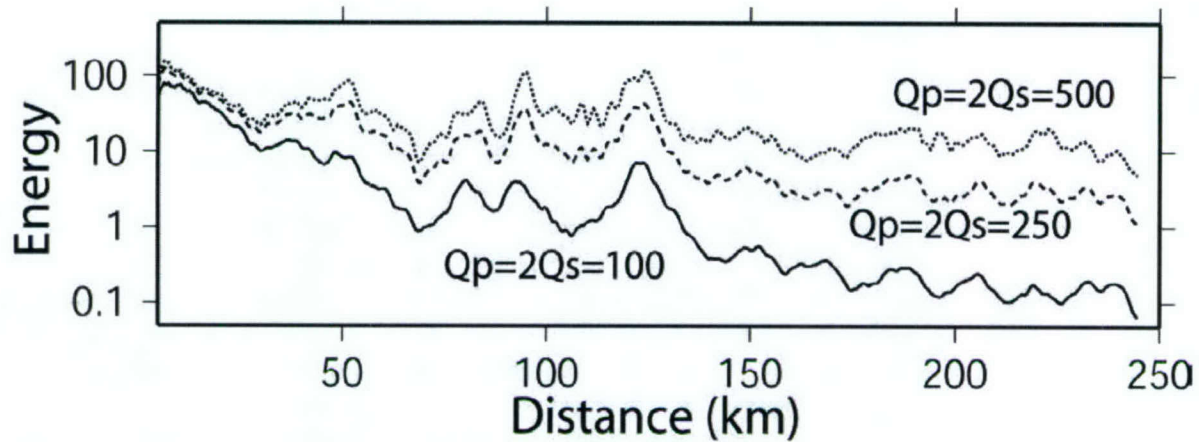
Figure 3.7 Synthetic P-SV Lg wave attenuation curves for the Flora-Asnes crust model. The intrinsic attenuation in the crust plays an important role for Lg energy attenuation.

3.3.3 P-SV Lg-wave propagation in the Flora-Asnes crust model.

For the P-SV wave case, we improved the stability of our complex screen propagator for long distance propagation. At the same time, we are working on the coupling between the body waves and the surface wave. Figure 3.7 shows the P-SV Lg wave attenuation versus distance. The 1-D background model is the Flora-Asnes crust model in the NORSAR region. A 10% RMS random velocity fluctuation with correlation lengths similar to the SH wave case is added to the background model. Three sets of P- and S-wave quality factors are used in the calculation. The results show that the intrinsic attenuation plays an important role in the Lg wave energy decay.

4. P-SV BOUNDARY ELEMENT METHOD FOR REGIONAL WAVE PROPAGATION

4.1 Background

Regional phases have long been recognized as important in the study of large-scale crustal structures, small-scale crustal heterogeneities, seismic sources, and determination of underground explosions and earthquakes. To improve path corrections as well as verify empirical observations, numerical simulations are needed to estimate the path effects on regional wave propagation. A number of regional numerical modeling methods have been developed to model Lg propagation behavior and path effects, depending on the complexity of the crust heterogeneity in the region considered. Finite-difference (FD) and finite-element (FE) methods are universal numerical techniques for simulation in general heterogeneous media. Because of the computational intensity, these full-waveform methods are often limited to the case of low frequencies for Lg simulation at regional distances. To reduce computation time, some alternative and flexible approaches, for example, ray diagrams (e.g., Bostock and Kennett, 1990; Keers *et al.*, 1996) and dynamic-ray-tracing method (Gibson and Campillo, 1994), have been used to obtain an intuitive understanding of path effects on Lg propagation. For large range Lg wave propagation, Wu et al. (1996, 2000) introduced a half-space GSP (Generalized Screen Propagator) for modeling the main characteristics of Lg (2-D *SH* case) in heterogeneous crustal waveguides. Later the method was extened to include the case of irregular surface topography (Wu and Wu, 2001)

Based on observations and numerical experiments, the large-scale crustal structures with variations in surface and Moho topography control the principal characteristics of Lg propagation. In contrast to the FD and FE methods, the boundary integral methods are more suitable for modeling complex reflection transmission effects across large-scale crustal structures with rugged surface/interface. For instance, the BE (boundary element) method provides a geometrically accurate description of irregular interfaces. Because the BE method is formulated in terms of integrals along boundaries, the traction-free condition for rugged free surface is easy and natural to treat in an accurate and stable manner. However, for regional waveguides up to a thousand kilometers, the BE method in the original form leads to very large sized matrixes and its inversion and implementation are prohibitively expensive. In a previous paper (Fu and Wu, 2001), an *SH* wavefield connection technique is developed by which the BE method can be used section by section for wave propagation at a far regional distance up to several thousand kilometers. The method takes the output of the previous section as the input of the next section in order to complete the entire crustal waveguide computation. The full-wave BE modeling is implemented within each section. The wavefield connection technique is used to couple the fields calculated in two adjoining sections. The division of sections is based on the complexity of crustal structures with a criterion of minimizing the possible multiple backscattering between sections. This section-by-section approach for long regional waveguides leads to significant computational savings in time and memory compared with the whole waveguide BE method. The section-by-section approach also leads to a hybrid modeling scheme of BE and GSP. The BE method is implemented in the frequency domain and has a kernel function compatible with the GSP method. In the hybrid scheme, the time-consuming BE method can be used to handle the sections with complicated boundary structures and severe surface topography. Subsequently the output will be used as the input to the GSP method for modeling the sections with a large volume of moderately heterogeneous media and mild topography. The hybrid method has been

applied to two crustal waveguide models from the Tibet region, one with *Lg* blockage and another without blockage (Fu and Wu, 2001).

The object of this section is to develop the *P-SV* wavefield connection technique for simulating elastic wave propagation in regional crustal waveguides. We first introduce integral equation representation for the crustal waveguide problems. We then briefly describe the principle of the elastic BE method and validate the computation programs using previously published results. We develop *P-SV* wavefield connection technique and test it using numerical experiments. Finally, we apply the section-by-section approach to *Lg* propagation simulations in long regional waveguides.
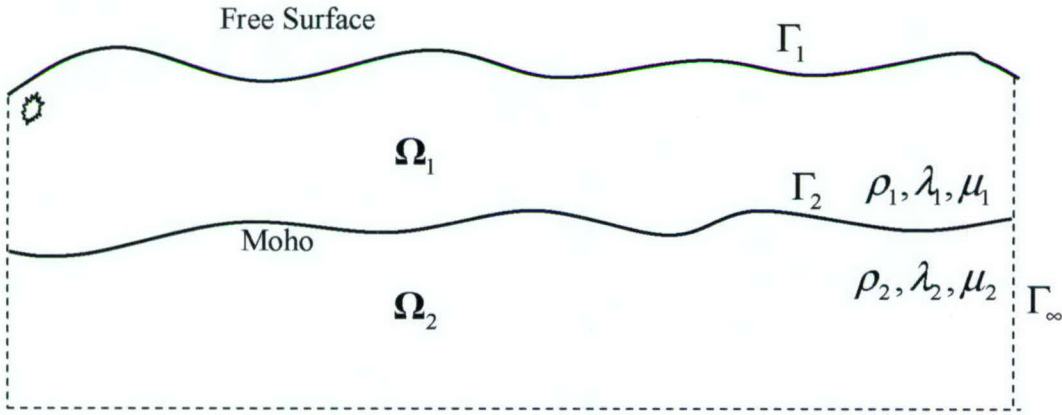

Figure 4.1 Geometry of a simplified crustal waveguide with irregular topographic and Moho interface

4.2 Boundary Integral Equation for Crustal Waveguide

Consider 2-D steady-state elastic wave propagation in a simplified crustal waveguide Ω_1 bounded by a rough free surface Γ_1 and an irregular Moho interface Γ_2. Figure 4.1 depicts the geometry of the problem. The waveguide medium is isotropic and homogeneous, described by the Lame constants and density (λ_1, μ_1, ρ_1). The displacement vector $\mathbf{u(r)}$ at a location $\mathbf{r}(x,z)$ satisfies the following elastic wave equation

$$\mu\nabla^2\mathbf{u(r)} + (\lambda + \mu)\nabla\nabla\cdot\mathbf{u(r)} + \rho\omega^2\mathbf{u(r)} = -\rho\mathbf{f}(\mathbf{r},\omega) \qquad (4.1)$$

where $\mathbf{f(r},\omega)$ is the body force occupying a region Ωs . $\mathbf{u(r)}$ also satisfies the traction-free boundary condition on Γ_1 and the continuity condition of displacement and traction across the Moho. The medium in the mantle Ω_2 is described by λ_2, μ_2, and ρ_2. We add two artificial boundaries Γ_∞ at the two truncated edges of the waveguide to form a closed solution domain $\Gamma = \Gamma_1 + \Gamma_2 + \Gamma_\infty$. Based on the representation theorem (e.g., Aki and Richards, 1980), equation (4.1) can be transformed into the following integral formulation:

$$\mathbf{C(r)u(r)} + \int_\Gamma \mathbf{u(r')}\Sigma(\mathbf{r,r'}) - \mathbf{t(r')}\mathbf{G(r,r')}]d\mathbf{r'} = \int_\Omega \rho\mathbf{f(r'},\omega)\mathbf{G(r,r')}d\mathbf{r'}, \qquad (4.2)$$

where $\mathbf{t(r)}$ is the traction vector, the coefficient $\mathbf{C(r)}$ generally depends on the local geometry at $\mathbf{r}$, and $\Sigma(\mathbf{r,r'})$ and $\mathbf{G(r,r')}$ are the fundamental solutions (Green's tensors) for displacements and tractions, respectively. $\mathbf{C(r)}, \Sigma(\mathbf{r,r'})$ and $\mathbf{G(r, r')}$ are 2×2 matrices for 2-D problems.

$$G_{ij} = \frac{i}{4\mu}\left(\psi\delta_{ij} - \phi\gamma_i\gamma_j\right)$$

$$\Sigma_{ij} = \frac{i}{4}\left[\left(\frac{\partial\psi}{\partial r} - \frac{\phi}{r}\right)\left(\delta_{ij}\gamma_k n_k + \gamma_j n_i\right) - \frac{2\phi}{r}\left(\gamma_i n_j - 2\gamma_i\gamma_j\gamma_k n_k\right) - 2\frac{\partial\phi}{\partial r}\gamma_i\gamma_j\gamma_k n_k + \left(\frac{\lambda}{\mu}\right)\left(\frac{\partial\psi}{\partial r} - \frac{\partial\phi}{\partial r} - \frac{\phi}{r}\right)\gamma_i n_j\right]$$

where

$$\psi = \left[H_0^{(1)}(k_s r) - \frac{1}{k_s r}\left(H_1^{(1)}(k_s r) - \frac{\beta}{\alpha}H_1^{(1)}(k_p r)\right)\right]$$

$$\phi = \left[\frac{\beta^2}{\alpha^2}H_2^{(1)}(k_p r) - H_2^{(1)}(k_s r)\right]$$

$k_s = \omega/\beta$ and $k_p = \omega/\alpha$, $\gamma_j = (r'_j - r_j)/r$

In this equation, $\mathbf{r}$ is the position of the observation points and $\mathbf{r}'$ is the position of the scattering points. For simplicity, the source distribution consists of a point source at $\mathbf{r}_0$ located inside Ω_1. The source integral over Ω_s in the right side of equation (4.2) can be reduced to

$$\int_\Omega \rho \mathbf{G}(\mathbf{r},\mathbf{r}')\mathbf{f}(\mathbf{r}',\omega)d\mathbf{r}' = \rho\mathbf{G}(\mathbf{r},r_0)\mathbf{f}(\omega) \tag{4.3}$$

where $\mathbf{f}(\omega)$ is the source spectrum vector.

The displacement Green's tensor $\mathbf{G}(\mathbf{r},\mathbf{r}')$ satisfies:

$$[(\lambda+\mu)\nabla\nabla\cdot + \mu\nabla^2]\mathbf{G}(\mathbf{r},\mathbf{r}') + \rho\omega^2\mathbf{G}(\mathbf{r},\mathbf{r}') = -\delta(\mathbf{r}-\mathbf{r}') \tag{4.4}$$

with the solution given by Morse and Feshbach (1953). The traction Green's tensor $\Sigma(\mathbf{r},\mathbf{r}')$ can be derived from $\mathbf{G}(\mathbf{r},\mathbf{r}')$ using Hooke's law. The boundary integral representation for wave propagation allows natural satisfaction of Sommerfeld radiation boundary conditions that are imposed on the far field behavior at infinity. No waves come back to Ω_1 through Γ_∞, that is, the following integral on Γ_∞ for the interior problem vanishes:

$$\int_{\Gamma_\infty}[\Sigma(\mathbf{r},\mathbf{r}')\mathbf{u}(\mathbf{r}') - \mathbf{G}(\mathbf{r},\mathbf{r}')\mathbf{t}(\mathbf{r},\mathbf{r}')]d\mathbf{r}' = 0, \quad \mathbf{r}\in\Omega_1 \tag{4.5}$$

For numerical calculations, truncating the waveguide has to be done and infinite boundary element absorbing boundary technique (Fu and Wu, 2000) should be applied to the elements at the truncating points on Γ_1 and Γ_2. Considering equation (4.3) and (4.5), and applying the traction-free condition to the free surface Γ_1, equation (4.2) for the interior problem in the crust (Region Ω_1) is simplified to

$$\mathbf{C}(\mathbf{r})\mathbf{u}(\mathbf{r}) + \int_{\Gamma_1}\Sigma(\mathbf{r},\mathbf{r}')\mathbf{u}(\mathbf{r}')]d\mathbf{r}' + \int_{\Gamma_2}\Sigma(\mathbf{r},\mathbf{r}')\mathbf{u}(\mathbf{r}') - \mathbf{G}(\mathbf{r},\mathbf{r}')\mathbf{t}(\mathbf{r}')]d\mathbf{r}' = \rho\mathbf{G}(\mathbf{r},\mathbf{r}_0)\mathbf{f}(\omega) \tag{4.6}$$

Equation (4.6) is a starting point for numerical implementation for wave propagation simulation. In order to solve $\mathbf{u}(\mathbf{r})$ and $\mathbf{t}(\mathbf{r})$ on Γ_2, we must build the corresponding boundary integral equation in Ω_2. The following integral formulation can be established for $\mathbf{r}\in\Omega_2$ bounded by a closed surface $\Gamma = \Gamma_2 + \Gamma_\infty$:

$$\mathbf{C}(\mathbf{r})\mathbf{u}(\mathbf{r}) + \int_\Gamma \Sigma(\mathbf{r},\mathbf{r}')\mathbf{u}(\mathbf{r}') - \mathbf{G}(\mathbf{r},\mathbf{r}')\mathbf{t}(\mathbf{r}')]d\mathbf{r}' = 0 \tag{4.7}$$

Similarly, the integration over the transparent artificial boundary Γ_∞ vanishes for the interior problem, simplifying equation (4.7) as

$$\mathbf{C}(\mathbf{r})\mathbf{u}(\mathbf{r}) + \int_{\Gamma_2}\Sigma(\mathbf{r},\mathbf{r}')\mathbf{u}(\mathbf{r}') - \mathbf{G}(\mathbf{r},\mathbf{r}')\mathbf{t}(\mathbf{r}')]d\mathbf{r}' = 0 \tag{4.8}$$

Equations (4.7) and (4.8) provide a description of the field through the crustal waveguide, making possible the simultaneous evaluation of the unknowns ($\mathbf{u}(\mathbf{r})$ on Γ_1 and) $\mathbf{u}(\mathbf{r})$ and $\mathbf{t}(\mathbf{r})$ on Γ_2) by using the continuity of displacement and traction across Γ_2 .

4.3 Boundary Element Method for Elastic Wave Simulation

The boundary integral representations described above can be used to calculate the field at any point inside Ω_1 once $\mathbf{u}(\mathbf{r})$ and $\mathbf{t}(\mathbf{r})$ are known on the boundaries. We use the BE method to solve the values of $\mathbf{u}(\mathbf{r})$ and $\mathbf{t}(\mathbf{r})$ on the boundaries. We discretize Γ_1 into L_1 elements and N_1 nodes, and Γ_2 into L_2 elements and N_2 nodes. The total node number is N. By using linear interpolation shape functions $\phi(\xi)$ in an element between the nodes I_1 and I_2, the variables $\mathbf{u}(\mathbf{r})$ and $\mathbf{t}(\mathbf{r})$ are approximated with the linear combination of their node values over the element, for example, (see Fig 4.1)

$$\mathbf{u}(\xi) = \sum_{l=I_1}^{I_2} \mathbf{u}(\mathbf{r}_l)\phi_l(\xi), \tag{4.9}$$

where ξ and l denote the local coordinate and local node index of an element. Using the following Kronecker delta function notation relating the local node code l of an element to the global node code j

$$\delta_{lj} = \begin{cases} 0, & l \neq j \\ 1, & l = j \end{cases} \tag{4.10}$$

we have

$$\mathbf{u}(\xi) = \sum_{j=1}^{N} \sum_{l=I_1}^{I_2} \mathbf{u}(\mathbf{r}_l)\phi_l(\xi)\delta_{lj} \tag{4.11}$$

Letting $\mathbf{C}_i = \mathbf{C}(\mathbf{r}_i)$ and $\mathbf{u}_i = \mathbf{u}(\mathbf{r}_i)$, equation (6) for $i=1$ to N is discretized into

$$\mathbf{C}_i \mathbf{u}_i + \sum_{j=1}^{N} \left\{ \sum_{e=1}^{L_1} \sum_{l=I_1}^{I_2} \left[\int_{\Gamma_e} \mathbf{\Sigma}(\mathbf{r}_i, \mathbf{r}'(\xi))\phi_l(\xi)d\mathbf{r}'(\xi) \right] \delta_{lj}\mathbf{u}_j + \sum_{e=1}^{L_2} \sum_{l=I_1}^{I_2} \left[\int_{\Gamma_e} \mathbf{\Sigma}(\mathbf{r}_i, \mathbf{r}'(\xi))\phi_l(\xi)d\mathbf{r}'(\xi) \right] \delta_{lj}\mathbf{u}_j \right.$$
$$\left. - \sum_{e=1}^{L_2} \sum_{l=I_1}^{I_2} \left[\int_{\Gamma_e} \mathbf{G}(\mathbf{r}_i, \mathbf{r}'(\xi))\phi_l(\xi)d\mathbf{r}'(\xi) \right] \delta_{lj}\mathbf{t}_j \right\} = \rho\mathbf{G}(\mathbf{r}_i, \mathbf{r}_0)f(\omega)$$

$$\tag{4.12}$$

which can be further rewritten as

$$\sum_{j=1}^{N} \left[\mathbf{h}_{ij}^{(1)}\mathbf{u}_j^{(1)} + \mathbf{h}_{ij}^{(2)}\mathbf{u}_j^{(2)} - \mathbf{g}_{ij}^{(2)}\mathbf{t}_j^{(2)} \right] = \rho\mathbf{G}(\mathbf{r}_i, \mathbf{r}_0)\mathbf{f}(\omega), \tag{4.13}$$

with

$$\mathbf{h}_{ij}^{(1)} = \sum_{e=1}^{L_1} \sum_{l=I_1}^{I_2} \int_{\Gamma_e} \left[\mathbf{\Sigma}(\mathbf{r}_i, \mathbf{r}'(\xi))\phi_l(\xi)d\mathbf{r}'(\xi) \right] \delta_{lj} + \mathbf{C}_j^{(1)}\delta_{ij}, \tag{4.14}$$

$$\mathbf{h}_{ij}^{(2)} = \sum_{e=1}^{L_2} \sum_{l=I_1}^{I_2} \int_{\Gamma_e} \left[\mathbf{\Sigma}(\mathbf{r}_i, \mathbf{r}'(\xi))\phi_l(\xi)d\mathbf{r}'(\xi) \right] \delta_{lj} + \mathbf{C}_j^{(2)}\delta_{ij}, \tag{4.15}$$

$$g_{ij}^{(2)} = \sum_{e=1}^{L_2} \sum_{l=I_1}^{I_2} \int_{\Gamma_e} [G(r_i, r'(\xi)) \phi_l(\xi) dr'(\xi)] \delta_{ij}, \tag{4.16}$$

In this expression $u_j^{(1)}$ is the displacement vector on the free surface Γ_1 and $u_j^{(2)}$ and $t_j^{(2)}$ are the displacement and traction vector on the Moho Γ_2. The coefficient matrices $h_{ij}^{(1)}$, $h_{ij}^{(2)}$ and $g_{ij}^{(2)}$, obtained by numerically integrating the product of the Green's tensors with interpolation shape functions over elements denotes a concentrated force generated at the jth scattering point on Γ and applied at the ith observation point. For $1 = i$ to N, equation (4.13) can be further compacted as a matrix equation:

$$H^{(1)}u^{(1)} + H^{(2)}u^{(2)} - G^{(2)}t^{(2)} = F, \tag{4.17}$$

where $F = \rho G(r_i, r_0) f(\omega)$. Similarly, equation (4.8) for $1 = i$ to N can be discretized and compacted as

$$\tilde{H}^{(2)}u^{(2)} - \tilde{G}^{(2)}t^{(2)} = 0, \tag{4.18}$$

where the coefficient matrices, $\tilde{H}^{(2)}$ and $\tilde{G}^{(2)}$, are calculated using the medium properties of the mantle Ω_2. A simultaneous system of matrix equations (4.7) and (4.8) can be assembled using the continuity of displacement and traction across Γ_2,

$$\begin{cases} u^{(1)} = u^{(2)} \\ t^{(1)} = t^{(2)} \end{cases}$$

by which the unknowns ($u(r)$ on Γ_1 and $u(r)$ and $t(r)$ on Γ_2) can be solved.

These matrices in equations (4.17) and (4.18) are full of complex coefficients which are functions of frequency, material property and geometry. The BE method described above can be directly extended to complex geological structures (Fu, 1996) for exploration-oriented seismic modeling. Since a large amount of matrix operations are involved and the matrix for each frequency component must be inverted, the BE method is computationally intensive at high frequencies for far regional waveguides. To improve computation speed, a variable element dimension technique can be adopted in the program implementation (Fu and Mu, 1994). Bouchon *et al.* (1995) suggested an approach of threshold criterion to make the coefficient matrices sparser by removing very small entries in the BE coefficient matrices. An efficient modification to the BE method can be made using the section-by-section approach with the wavefield connection technique developed in this study.

The computation program of the elastic wave BE method described above is tested by dimensionless frequency responses of a semi-circular canyon with radius a. The previously published results (Sánchez-Sesma et *al.*, 1985; Sánchez-Sesma and Campillo, 1991) for this typical topographic structure are used for comparison. The two sharp edges at $x = \pm a$ provide a crucial target to validate various numerical methods. Figure 4.2 shows the comparison with good agreement in both horizontal and vertical amplitudes between our results (solid lines) and the

Sánchez-Sesma & Campillo's solutions for vertically incident plane P waves and for various normalized frequencies η defined as $\eta = l/2a$, where l is the wavelength. Poisson's ratio is assumed to be $1/3$. We can see some minor departures because of different element approximations used by these two numerical methods. Fewer elements per wavelength will reduce the size of the resultant coefficient matrices. To determine an applicable element number per wavelength, the comparisons for $0°$ incidence and $\eta = 1.0$ are given in Figure 4.3 for different discretization rates of points per wavelength to discretize the arc of the semicircular canyon. We see that sampling at three points per wavelength could be used for general applications.
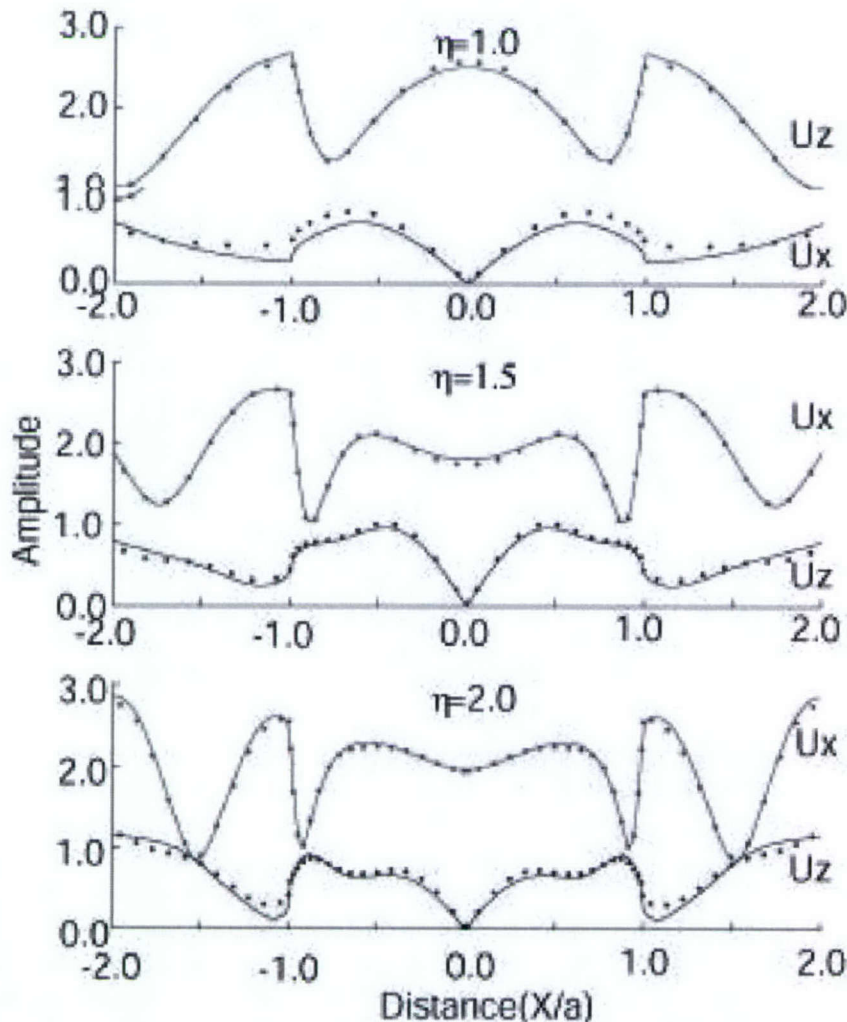

Figure 4.2: The horizontal and vertical amplitude response by our method (solid line) and Sanchez-Sesma & Campillo (1991) (dotted line) of a semicircular canyon topography to vertically incident P waves for various dimensionless frequency η
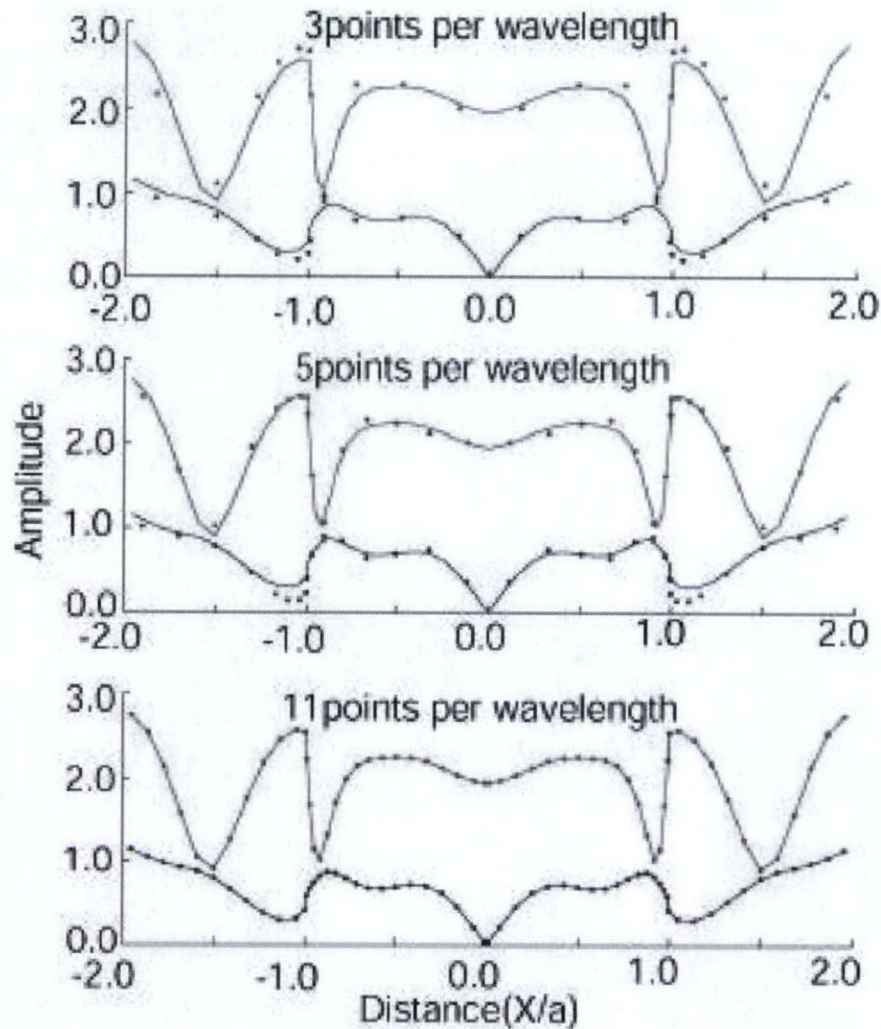
Figure 4.3: The horizontal and vertical amplitude responses of a semicircular canyon topography to vertically incident P waves and $\eta = 1.0$ with the solid lines for 21 points per wavelength and the dots for various sampling rates.

The comparisons above confirm the validity of our formulation and computation code. We now demonstrate the applicability of our program by synthesizing wave propagation through a single-layer crustal waveguide with flat free surface. The homogeneous waveguide shown in Figure 4.4 is 100 km long and 32 km thick, overlaying a flat mantle half-space. The point explosive source is located on the left boundary at 2.0-km depth. Figure 4.5 shows the synthetic seismograms calculated in the frequency range of 0-4.5 Hz, with receivers at 1-km spacing along a vertical profile at the distance of 80 km from the source. We see that for elastic wave propagation this simple waveguide with both flat topography and flat Moho leads to complex superposition of various waves, demonstrating the development of converted waves as well as

40

the formation of guided waves as repetitive reflections at both the free surface and Moho. In terms of propagation paths (see Figure 4.4), we can identify three major systems of waves generated in the waveguide. As shown in Fig 4.5, the direct *P*-wave from the source to receivers carries a major part of the source energy in this flat boundary waveguide. The *P*-wave incident upon the free surface and the Moho at oblique angles generates two systems of waves, one set off at the free surface and another off at the Moho. These two systems of waves and their converted waves bounce back and forth between the free surface and the Moho. Since no scattering mechanism is present in the waveguide, the constructive interference of repeatedly reflected waves presents a checkerboard-like pattern (Jih, 1996) that adequately explains the formation of crustal guided waves either as multiple reflections or as higher-modes.
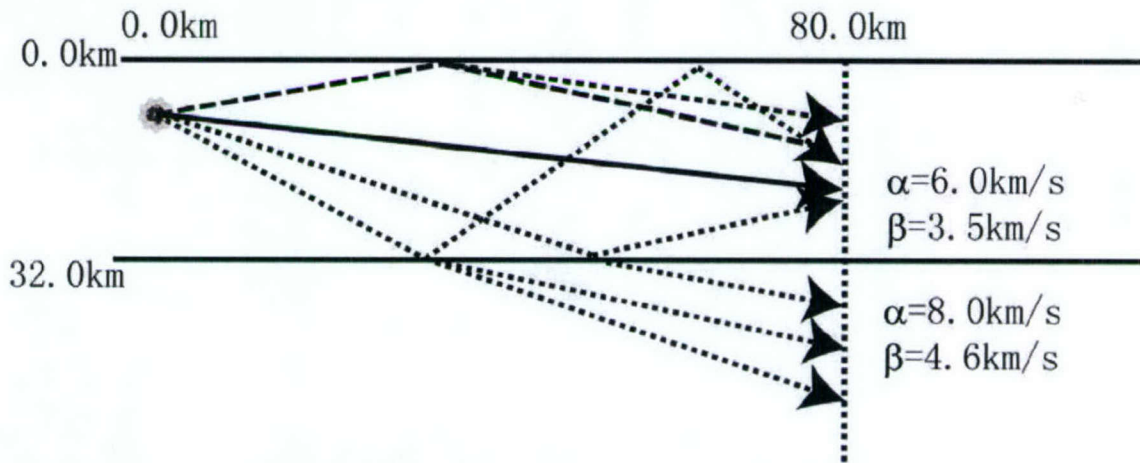
Figure 4.4: A single-layer flat crustal waveguide with the explosive source at 2-km depth. The wave generated in the waveguide are grouped into three systems: the first directly from the source to the receivers (solid line), the second off at the free surface (dash lines) and the third off the Moho (dotted lines).
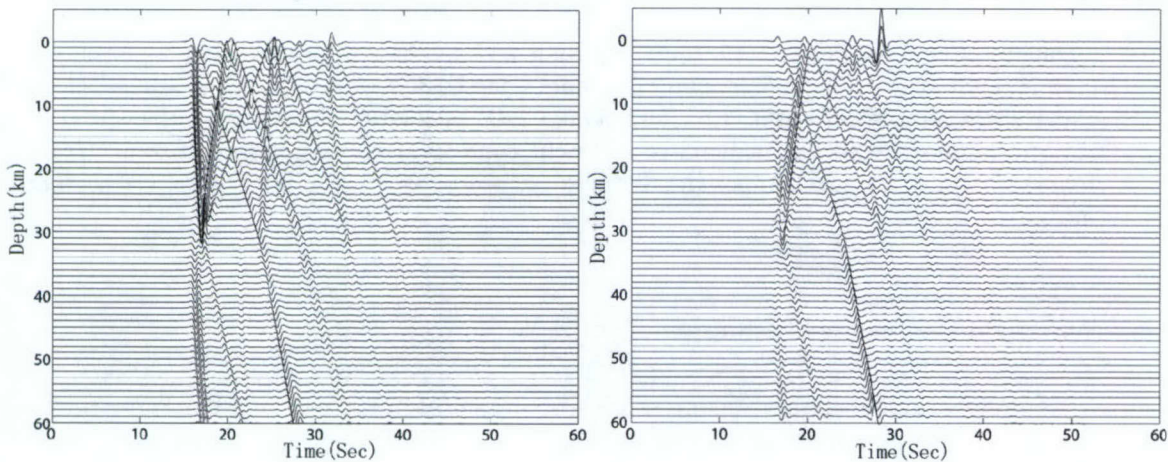
Figure 4.5: Synthetic seismograms for receivers at 1-km spacing along a vertical profile at 80km for a point source. The horizontal (left panel) and vertical (right panel) components are computed in the frequency range of 0-3.5hz.

41
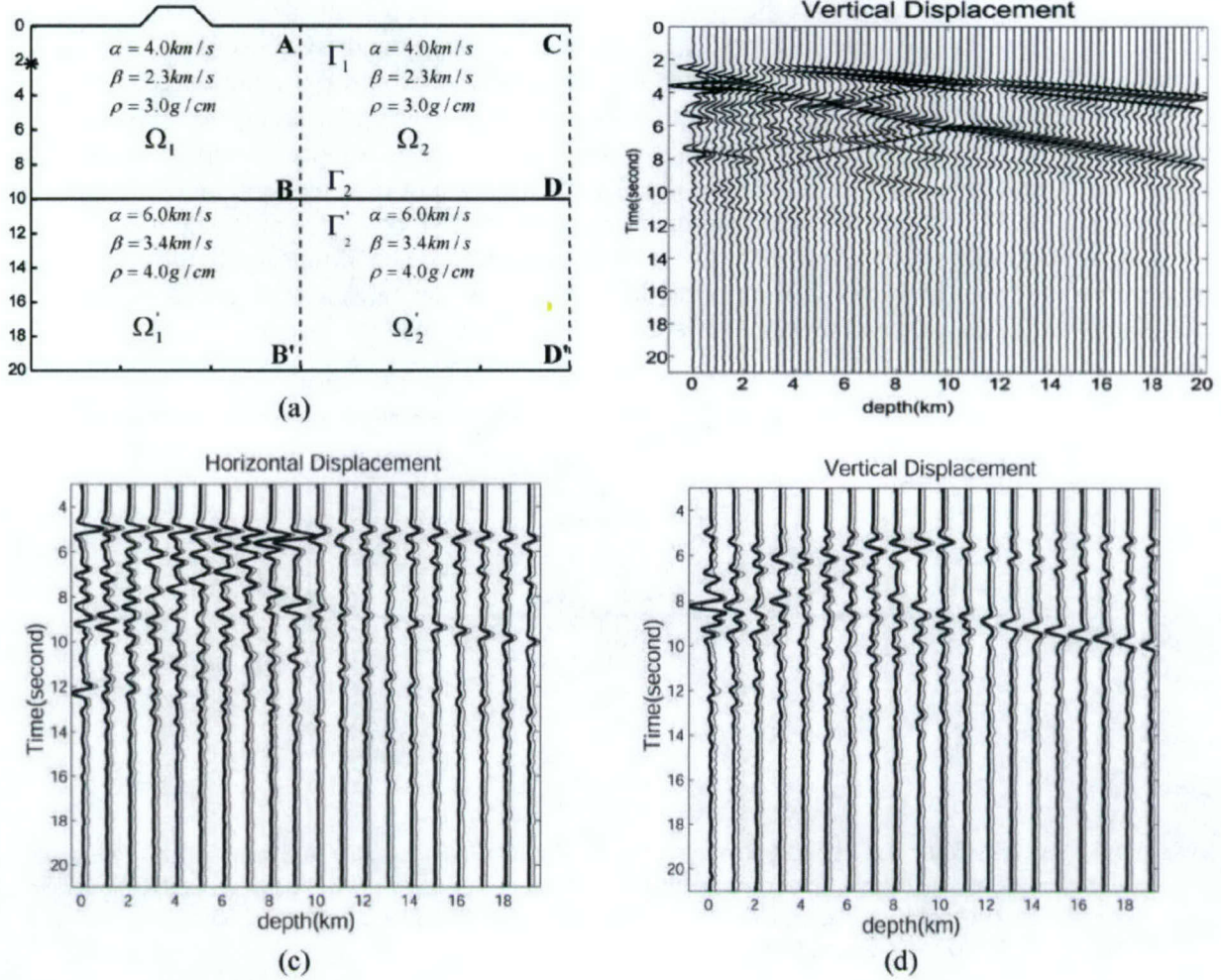
Figure 4.6: The boundary connection technique. (A) the diagrams show the connection formulation. (B) the vertical incident wavefield along the connecting boundary ABB' , (C) comparison of the horizontal component of the wavefield along CDD' calculated directly from the source (thick lines) and the wavefield calculated using the connection technique (thin lines). (D) Comparison of the vertical component. The comparison shows the validity of the connection technique.

4.4 P-SV Wavefield Connection Technique

We aim to develop a section-by-section approach for simulating wave propagation in regional waveguides to reduce the computation cost of extremely large matrix operations. Wavefield connection technique couples the fields between two adjacent sections. The connection configuration is illustrated in Figure 4.6(A). An artificial boundary is introduced as a wavefield connection boundary to a crustal waveguide consisting of an irregular free surface Γ_1 and an interface Γ_2 . The waveguide is divided into four subdomains, Ω_1, Ω_2 in the crust, and Ω_1', Ω_2' in

the mantle. The left boundaries of Ω_1 and $\Omega_1^{'}$, and the right boundaries of Ω_2 and $\Omega_2^{'}$ are assumed to extend to infinity at left and right respectively. The fields in Ω_1 and $\Omega_1^{'}$, can be calculated from the first section. Its output field $\mathbf{u}_0(\mathbf{r})$ on the connection boundary $\Gamma_{AB'}$ will be used to satisfy the boundary condition when the BE method is used to calculate wave propagation in Ω_2 and $\Omega_2^{'}$. The output field is received along the next connection interface $\Gamma_{CD'}$, and will be used as the input to the next propagation. With the initial field $\mathbf{u}_0(\mathbf{r})$ known on the connection boundary $\Gamma_{AB'}$ now we analyze wave scattering in Ω_2, $\Omega_2^{'}$ in order to build boundary integral equations for wave propagation in these sections. Apparently, all the space points of Ω_2, $\Omega_2^{'}$ except on $\Gamma_{AB'}$ can only receive the scattered field. Therefore, the total field $\mathbf{u}(\mathbf{r})$ on the boundaries of Ω_2 and $\Omega_2^{'}$ is composed of

$$\mathbf{u}(\mathbf{r}) = \begin{cases} \mathbf{u}_0(\mathbf{r}) + \mathbf{u}_s(\mathbf{r}) & \mathbf{r} \in \Gamma_{AB'} \\ \mathbf{u}_s(\mathbf{r}) & \mathbf{r} \notin \Gamma_{AB'} \end{cases} \tag{4.19}$$

Applying the traction-free condition to the free surface Γ_1 , the boundary integral equation can be built for $\mathbf{r} \in \Omega_2$ and $\mathbf{r} \notin \Gamma_{AB'}$

$$\mathbf{C}(\mathbf{r})\mathbf{u}_s(\mathbf{r}) + \int_{\Gamma_1+\Gamma_2} \Sigma(\mathbf{r},\mathbf{r}')\mathbf{u}_s(\mathbf{r}')d\mathbf{r}' + \int_{\Gamma_{AB}} \Sigma(\mathbf{r},\mathbf{r}')[\mathbf{u}_0(\mathbf{r}') + \mathbf{u}_s(\mathbf{r}')]d\mathbf{r}' + \int_{\Gamma_{CD}} \Sigma(\mathbf{r},\mathbf{r}')\mathbf{u}_s(\mathbf{r}')d\mathbf{r}'$$
$$= \int_{\Gamma_2} \mathbf{G}(\mathbf{r},\mathbf{r}')\mathbf{t}_s(\mathbf{r}')d\mathbf{r}' + \int_{\Gamma_{AB}} \mathbf{G}(\mathbf{r},\mathbf{r}')[(\mathbf{t}_0(\mathbf{r}') + \mathbf{t}_s(\mathbf{r}')]d\mathbf{r}' + \int_{\Gamma_{CD}} \mathbf{G}(\mathbf{r},\mathbf{r}')\mathbf{t}_s(\mathbf{r}')d\mathbf{r}' \tag{4.20}$$

The artificial boundaries Γ_{AB} and Γ_{CD} are assumed to be transparent, implying the outward energy radiation across Γ_{AB} and Γ_{CD} should always be in the outward direction with no reflection returning to Ω_2 . Therefore, there is no energy contribution scattering from Γ_{AB} and Γ_{CD} , that is,

$$\int_{\Gamma_{AB}} [\Sigma(\mathbf{r},\mathbf{r}')\mathbf{u}_s(\mathbf{r}') - \mathbf{G}(\mathbf{r},\mathbf{r}')\mathbf{t}_s(\mathbf{r}')]d\mathbf{r}' = 0, \qquad \mathbf{r} \in \Omega_2 \tag{4.21}$$

and

$$\int_{\Gamma_{CD}} [\Sigma(\mathbf{r},\mathbf{r}')\mathbf{u}_s(\mathbf{r}') - \mathbf{G}(\mathbf{r},\mathbf{r}')\mathbf{t}_s(\mathbf{r}')]d\mathbf{r}' = 0 \qquad \mathbf{r} \in \Omega_2 \tag{4.22}$$

Scattering from the artificial truncated points, A, B, C, and D, can be handled using an infinite element absorbing boundary technique (Fu and Wu, 2000). Therefore, equation (4.20) is reduced to

$$\mathbf{C}(\mathbf{r})\mathbf{u}_s(\mathbf{r}) + \int_{\Gamma_1} \Sigma(\mathbf{r},\mathbf{r}')\mathbf{u}_s(\mathbf{r}')d\mathbf{r}' + \int_{\Gamma_2} [\Sigma(\mathbf{r},\mathbf{r}')\mathbf{u}_s(\mathbf{r}') - \mathbf{G}(\mathbf{r},\mathbf{r}')\mathbf{t}_s(\mathbf{r}')]d\mathbf{r}'$$
$$= \int_{\Gamma_{AB}} [(\mathbf{G}(\mathbf{r},\mathbf{r}')\mathbf{t}_0(\mathbf{r}') - \Sigma(\mathbf{r},\mathbf{r}')\mathbf{u}_0(\mathbf{r}')]d\mathbf{r}' \tag{4.23}$$

In equation (4.23), both the initial displacement and traction on the connection boundary are assumed to be known. $\mathbf{u}_0(\mathbf{r})$ can be calculated from the previous section, incident traction $\mathbf{t}_0(\mathbf{r})$ can also be calculated from the previous section. Alternatively, we can use the elastic Rayleigh integrals (Wu, 1989) which contain either the displacement or the traction field. We can reduce the surface integral in the right side of equation (4.23) to the elastic wave Rayleigh integral that only contains the initial displacement $\mathbf{u}_0(\mathbf{r})$:

43

$$\mathbf{C}(\mathbf{r})\mathbf{u}_s(\mathbf{r}) + \int_{\Gamma_1}\Sigma(\mathbf{r},\mathbf{r}')\mathbf{u}_s(\mathbf{r}')d\mathbf{r}' + \int_{\Gamma_2}[\Sigma(\mathbf{r},\mathbf{r}')\mathbf{u}_s(\mathbf{r}') - \mathbf{G}(\mathbf{r},\mathbf{r}')\mathbf{t}_s(\mathbf{r}')]d\mathbf{r}' = -2\int_{\Gamma_{AB}}\Sigma(\mathbf{r},\mathbf{r}')\mathbf{u}_0(\mathbf{r}')d\mathbf{r}'$$
(4.24)

where $\Sigma(\mathbf{r},\mathbf{r}')$ is related to $\mathbf{G}(\mathbf{r},\mathbf{r}')$ by Hooke's law:

$$\Sigma(\mathbf{r},\mathbf{r}') = \lambda\mathbf{I}(\nabla\cdot\mathbf{G}(\mathbf{r},\mathbf{r}')) + \mu(\nabla\mathbf{G}(\mathbf{r},\mathbf{r}') + \mathbf{G}(\mathbf{r},\mathbf{r}')\nabla),$$
(4.25)

where $\mathbf{I}$ is the unit dyadic and $\mathbf{G}(\mathbf{r},\mathbf{r}')\nabla$ is the transpose of $\nabla\mathbf{G}(\mathbf{r},\mathbf{r}')$ with respect to the corresponding coordinates. For analytic expressions of $\mathbf{G}$ and Σ in isotropic homogeneous elastic media, see Wu (1994, Appendix)

We see that the unknowns in equation (4.24) are $\mathbf{u}_s(\mathbf{r})$ on Γ_1 and $\mathbf{u}_s(\mathbf{r})\,\&\,\mathbf{t}_s(\mathbf{r})$ on Γ_2. In order to solve $\mathbf{u}_s(\mathbf{r})\,\&\,\mathbf{t}_s(\mathbf{r})$, we must build the corresponding boundary integral equation in sub-domain Ω_2':

$$\mathbf{C}(\mathbf{r})\mathbf{u}_s(\mathbf{r}) + \int_{\Gamma_2'}\Sigma(\mathbf{r},\mathbf{r}')\mathbf{u}_s(\mathbf{r}')d\mathbf{r}' + \int_{\Gamma_{BB'}}\Sigma(\mathbf{r},\mathbf{r}')[(\mathbf{u}_0(\mathbf{r}') + \mathbf{u}_s(\mathbf{r}')]d\mathbf{r}' + \int_{\Gamma_{DD'}}\Sigma(\mathbf{r},\mathbf{r}')\mathbf{u}_0(\mathbf{r}')d\mathbf{r}'$$
$$= \int_{\Gamma_2'}\mathbf{G}(\mathbf{r},\mathbf{r}')\mathbf{t}_s(\mathbf{r}')d\mathbf{r}' + \int_{\Gamma_{BB'}}\mathbf{G}(\mathbf{r},\mathbf{r}')[(\mathbf{t}_0(\mathbf{r}') + \mathbf{t}_s(\mathbf{r}')]d\mathbf{r}' + \int_{\Gamma_{DD'}}\mathbf{G}(\mathbf{r},\mathbf{r}')\mathbf{t}_0(\mathbf{r}')d\mathbf{r}' \quad (4.26)$$

where a sufficient long boundary $\Gamma_{BB'}$ is used with its end set as an infinite element. Similarly, since there is no discontinuity across $\Gamma_{BB'}$ and $\Gamma_{DD'}$, we can assume $\Gamma_{BB'}$ and $\Gamma_{DD'}$ to be transparent and reduce equation (4.26) to

$$\mathbf{C}(\mathbf{r})\mathbf{u}_s(\mathbf{r}) + \int_{\Gamma_2'}[\Sigma(\mathbf{r},\mathbf{r}')\mathbf{u}_s(\mathbf{r}') - \mathbf{G}(\mathbf{r},\mathbf{r}')\mathbf{t}_s(\mathbf{r}')]d\mathbf{r}' = \int_{\Gamma_{BB'}}[\mathbf{G}(\mathbf{r},\mathbf{r}')\mathbf{t}_0(\mathbf{r}') - \Sigma(\mathbf{r},\mathbf{r}')\mathbf{u}_0(\mathbf{r}')]d\mathbf{r}' \quad (4.27)$$

The integration term containing the initial traction $\mathbf{t}_0(\mathbf{r})$ in the right side of equation (4.27) can be removed using the elastic wave Rayleigh integral representation, yielding

$$\mathbf{C}(\mathbf{r})\mathbf{u}_s(\mathbf{r}) + \int_{\Gamma_2'}[\Sigma(\mathbf{r},\mathbf{r}')\mathbf{u}_s(\mathbf{r}') - \mathbf{G}(\mathbf{r},\mathbf{r}')\mathbf{t}_s(\mathbf{r}')]d\mathbf{r}' = -2\int_{\Gamma_{BB'}}\Sigma(\mathbf{r},\mathbf{r}')\mathbf{u}_0(\mathbf{r}')d\mathbf{r}'$$
(4.28)

The continuity of displacement and traction across interface Γ_{BD} is employed when equations (4.24) and (4.28) are combined to solve the problem. By solving the joint boundary integral equations of Ω_2 and Ω_2', we can obtain the wavefields $\mathbf{u}_s(\mathbf{r})$ on Γ_1, $\mathbf{u}_s(\mathbf{r})$ and $\mathbf{t}_s(\mathbf{r})$ on Γ_2. The observed field along $\Gamma_{CD'}$ is calculated explicitly from the fields on the boundaries.

4.5 Validation for P-SV Connection Technique

To test the validity of the connection technique we present a comparison between the wave field obtained using the BE method to directly calculate wave propagation from the source to the observation surface $\Gamma_{CD'}$ and the one calculated by the connection scheme (Fig 4.6). In both cases the source time function are the same, with a dominant frequency of 1 Hz. First the

44

intermediate wave field (Fig 4.6 (B)) on $\Gamma_{AB'}$ calculated from the source is used as the incident field. Then the BE method is used to calculate wave propagation from $\Gamma_{AB'}$ to $\Gamma_{CD'}$. The dominant arrivals for the incident field at $\Gamma_{AB'}$ consist of direct P wave, pS, pP, and multi-reflection between the two layers. More multiply reflected waves between the free surface and the interface can be clearly seen in the seismograms at $\Gamma_{CD'}$. The excellent agreement between the wavefield calculated by the two methods shown in Figure 4.6(C) and 4.6(D) confirms the validity of the connection technique.
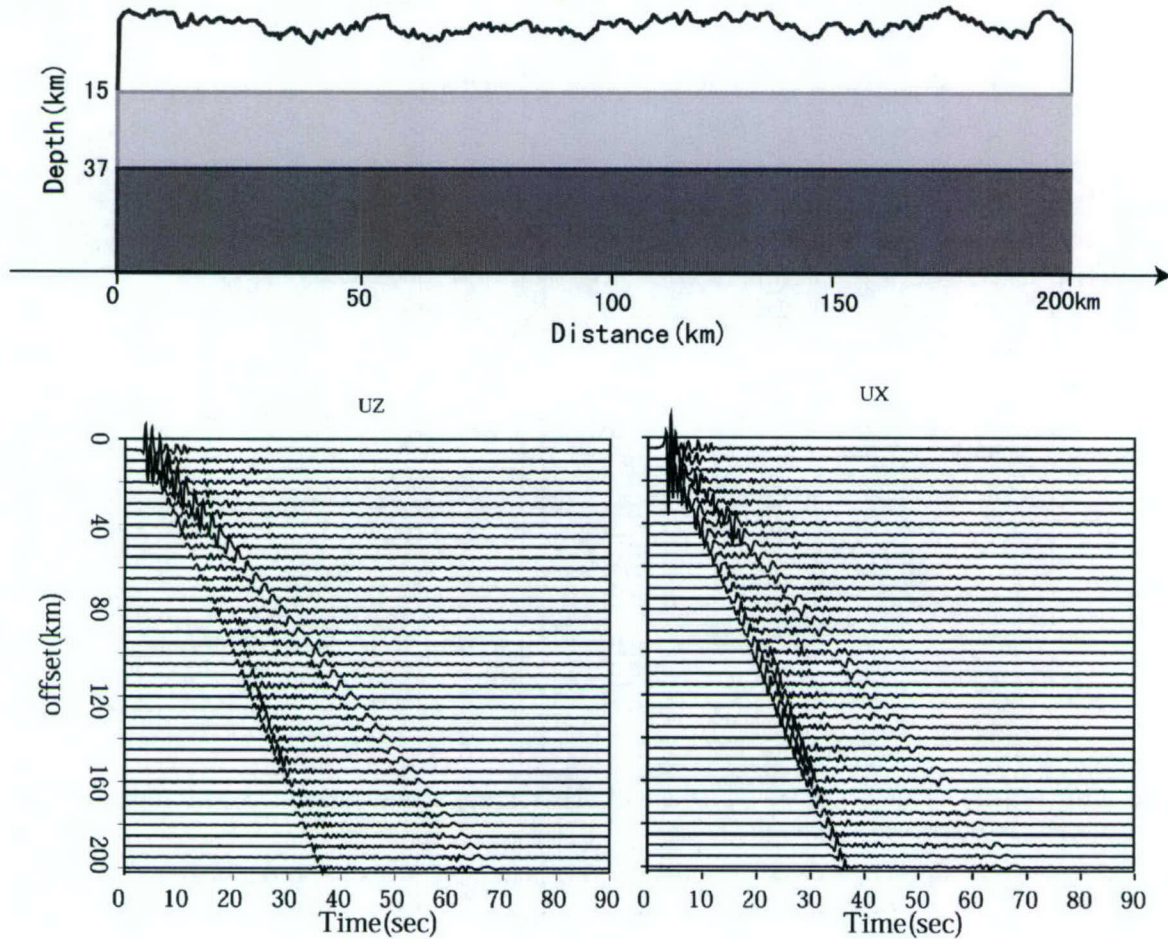
Figure 4.7 Synthetic seismogram for two-layer crustal model with random topography. The source is located at the depth of 2 km. The topographic fluctuation has an exponential correlation function with a RMS of 0.5 km and a correlation length of 5km. We can see both forscattering and backscattering in the seismogram.

4.6 Numerical Examples and Applications

We use the BE connection technique given above to calculate the wave fields of several models with rough topography. The basic model is a two-layer crust over a half space. The parameters for this model are listed in Table 4.1. The model has two discontinuities at the depth of 15 km

45

and 37 km. The receivers are along the surface. An explosive source is located at the depth of 2 km, and the source time function is a Ricker wavelet with a dominant frequency of 1 Hz. Figure 4.7 shows the synthetic seismogram for this model with an irregular topography. The correlation length of the topographic fluctuation is 5 km and the RMS amplitude is 0.5 km. Comparing to the wave field (Fig. 4.8) for the model with a flat surface, we can see that the amplitudes of direct P wave and Rayleigh wave are relatively small due to the scattering effect of the rough topography. Both fore-scattering and back-scattering waves can be seen in Fig 4.7.

Table 4.1: Crust velocity model

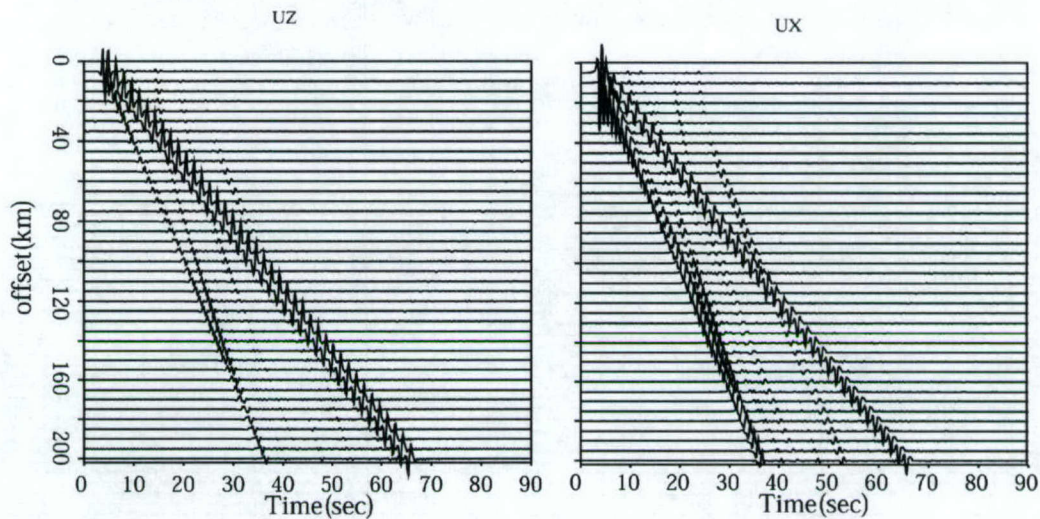| Thickness (km)	Vp (km/s)	Vs (km/s)	$\rho(g/cm^3)$
15.00	6.00	3.46	2.80
22.00	6.51	3.76	3.00
Infinity	8.05	4.65	3.30

Figure 4.8 Synthetic seismogram for a model with flat surface. Multi-reflected waves and Rayleigh waves can be clearly seen in the figure.

We calculated the energy attenuation curves for these models. Figure 4.9 shows the energy attenuation vs. distance. The one at the bottom is the energy in the whole seismogram. The energy is lost due to the topography scattering. We calculated random topography with exponential and Gaussian distribution with 0.4 km RMS and 1.0 km RMS. We can see that exponential topography is more effective than the Gaussian topography in attenuating the wave energy. In addition, the larger the topographic fluctuation is, the stronger the scattering. Now we apply our connection technique to regional wave propagation simulations in a synthetic model. As shown in Figure 4.10(a), the model is a laterally varying crustal model with a 600 km range. The model is divided into three 200 km segments. The first segment is a 200 km waveguide with a Gaussian hill which is given by

$$h(x) = -h_0 \exp\left(-\frac{(x-x_0)^2}{2\sigma^2}\right)$$

46

where x_0=62 km, h_0=4 km, σ=9.129 km. The second section has a waveguide necking, the height of the step is 7 km. The third part is a waveguide with random topography which has a Gaussian correlation function with a correlation length of 5 km and the RMS height is 0.6 km. The point source is located at 8 km depth. The receivers are along both the free surface and vertical profiles. The computation are in the frequency range of 0-2.5 Hz. We first calculate wave propagation from source to produce the incident wave field on the first connection boundary Γ_1 (Fig 4.10(b)), the multi-reflected waves, converted waves, head waves and Rayleigh waves can all be clearly seen in the figure. Subsequently the BE method is used to calculate wave propagation in the second section and obtain the wave field on the second connection boundary Γ_2 (Fig 4.10(c)). Finally we use the wave field on Γ_2 as the incident field and calculate the wavefield in the third section. Fig 4.10(d) shows the horizontal wavefield on Γ_3, we can see from the scattering effect of the random topography, the Rayleigh waves are mostly scattered and some coda waves appear. We put the wavefield along the surface obtained from the three sections together in Fig 4.10(e). Fig 4.10(f) is the energy attenuation along the surface. On the surface of the hill, the energy is relatively low compared to the vicinal area. Furthermore, the topography has great effect on the energy attenuation.
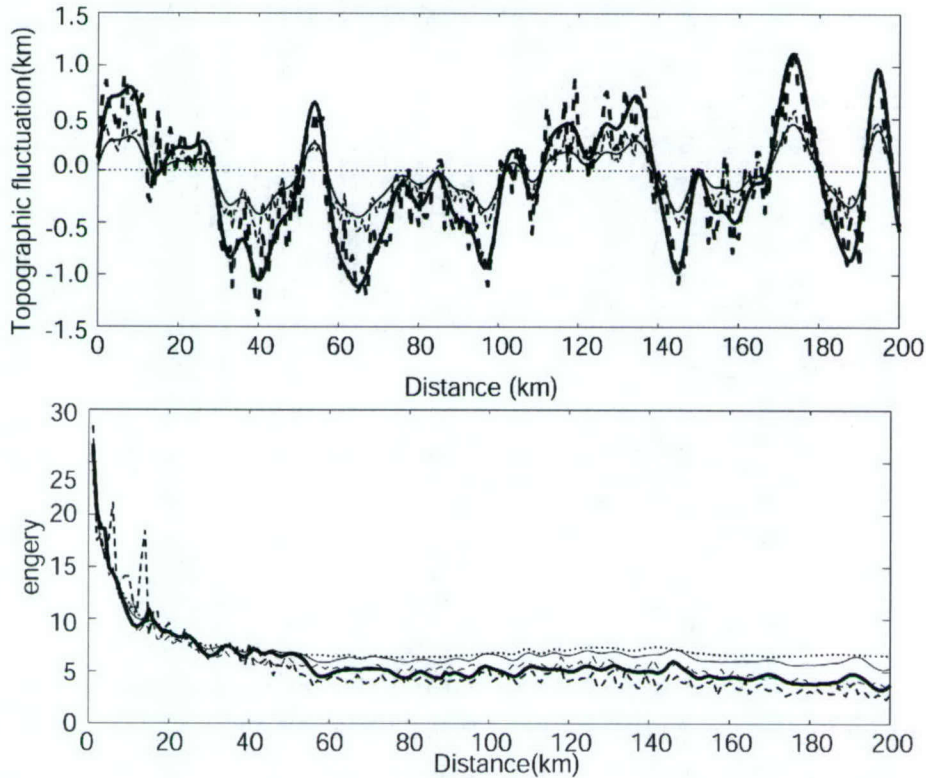
Figure 4.9: Energy attenuation for earth models with different topographies. On the top is the topography used in our calculation, the thick solid line is a Gaussian random topographic with a RMS of 0.5 km, thin solid line is a Gaussian random topography with RMS of 0.25 km, the thick dash line is exponential random topography with RMS of 0.5 km and the thin dash line is exponential random topography with rms of 0.25 km, while the reference model (flat surface) is shown in dotted line. On the bottom are the energy attenuation curves for the entire propagation distance, the lines are the same mean as those in the top figure.

Figure 4.10 Application to a large model. (a) The model; (b) horizontal wavefield on Γ_1 ; (c) horizontal wavefield on Γ_2 ; (d) horizontal wavefield on ; Γ_3 (e) horizontal wavefield along the surface; and (d) energy attenuation along the surface.
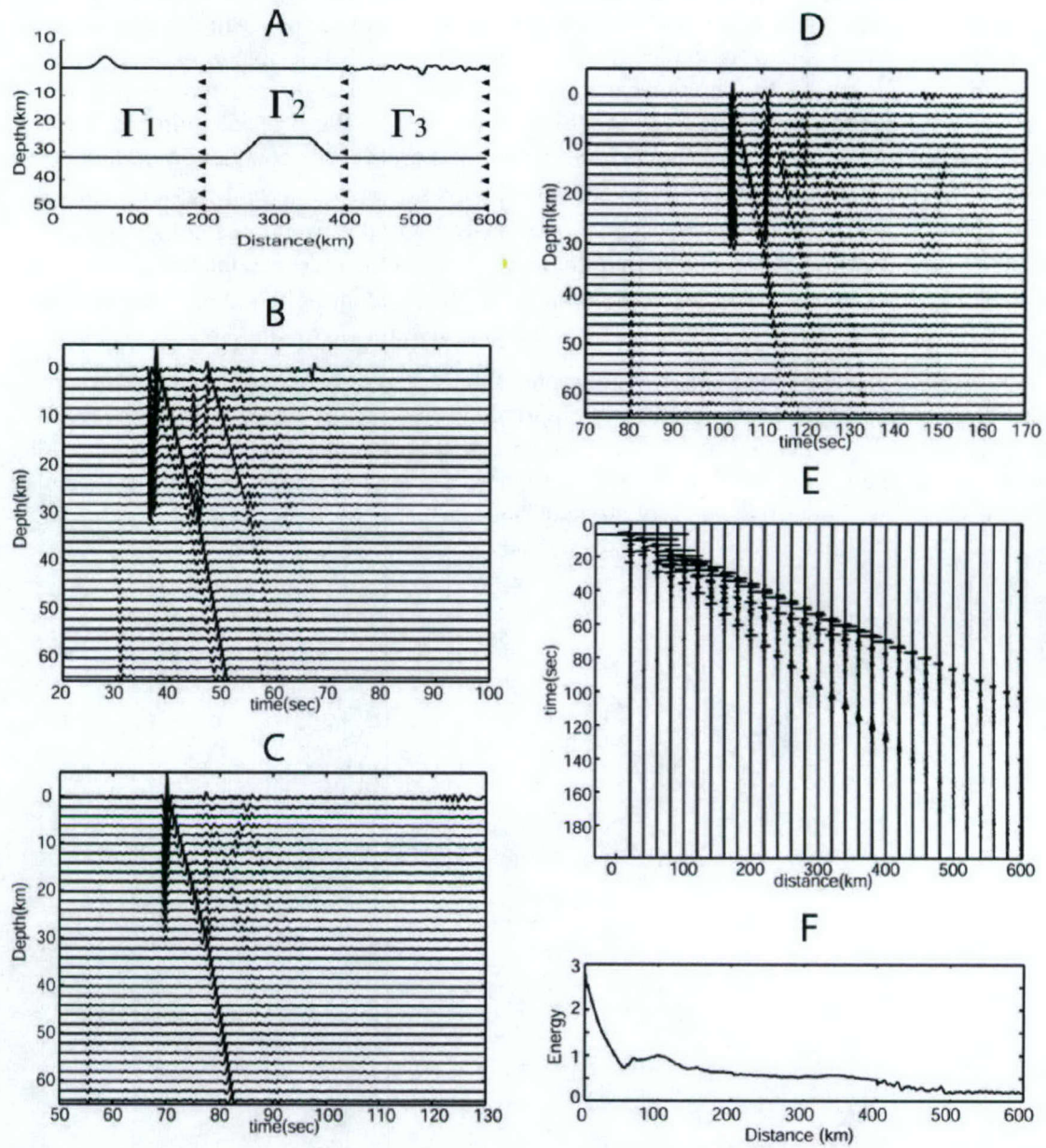
5. ACKNOWLEDGEMENT

6. REFERENCES

Aki, K., 1980. Scattering and attenuation of shear waves in the lithosphere, *J. Geophys. Res.*, 85, 496-6504.

Aki, K. and Richards, P.G., 1980. *Quantitative Seismology.* Theory and Methods, W.H. Freeman, San Francisco.

App, F.N., Bos, R.J., and Kamm, J.R., 1996, Synthetic seismograms at regional distances for May 1995 Earthquake and Explosion source in Western China, *Proceedings of the 18th Annual Seismic Research Symposium on Monitoring a Comprehensive Nuclear-Test-Ban Treaty*, 119-128, September 4-6.

Archambeau, C, Orrey, J., and Kohl, B., 1996, 3-D seismic wave synthesis and full wavefield inversion, *Proceedings of the 18th Annual Seismic Research Symposium on Monitoring a Comprehensive Nuclear-Test-Ban Treaty*, 129-138, September 4-6.

Baumgardt, D.R., 1990. Investigation of teleseismic Lg blockage and scattering using regional arrays, *Bull. Seis. Soc. Am.*, 80, 2261-2281.

Bonner, J.B., H.J. Patton, A.C. Rosca, H. Hooper, J. Orrey, M. Leidig and I. Gupta, (2003), Aspects of Rg and Lg generation from the Shagan depth of burial explosions, *Proceedings of the 25th Seismic Research Review, Nuclear Explosion Monitoring: Building the Knowledge Base*, 384-394.

Bostock, M. G., and Kennett, B. L. N., 1990, The effect of three-dimensional structure on Lg propagation patterns, *Geophys. J. Int.* 101, 355-365.

Bouchon, M., 1982, The complete synthesis of seismic crustal phases at regional distances, *J. Geophys. Res.*, 78, 1735-1741.

Bouchon, M., et al. (1985), Theoretical modeling of Lg wave attenuation, in *The VELA Program; A Twenty-five Year Review of Basic Research.*

Bouchon, M., Schultz, C.A. & Toksöz, M.N., 1995. A fast implementation of boundary integral equation methods to calculate the propagation of seismic waves in laterally varying layered media, *Bull. Seis. Soc. Am.* 85, 1679-1687.

Bradley, C.R. and Jones, E.M., 1998, Modeling propagation effects from explosion in Western China and India, *Proceedings of the 20th Annual Seismic Research Symposium on Monitoring a Comprehensive Nuclear-Test-Ban Treaty*, 173-181, September 21-23.

Bradley, C.R. and Jones, L.E., 1999, Full waveform modeling of the effects of Q and structure over sub-regional paths in Western China}, Proceedings of the 21st Annual Seismic Research Symposium on Monitoring a Comprehensive Nuclear-Test-Ban Treaty, 28-38, September 21-24.Campillo, M., 1990. *Propagation and attenuation characteristics of the crustal phase Lg, Pure and Applied Geophysics*, 132, 1-19.

Campillo, M., M. Bouchon, and B. Massinon, 1984, Theoretical study of the excitation, spectral characteristics, and geometrical attenuation of regional seismic phases, *Bull. Seism. Soc. Am.*, 74, 79-90.

Campillo, M., 1990, Propagation and attenuation characteristics of the crustal phase Lg, *Pure and Appl. Geophys.*, 132, 1-19.

Campillo, M. & Paul, A., 1992. Influence of the lower crustal structure on the earth coda of regional seismograms, *J. Geophys. Res.*, 97, 3405-3416.

Campillo, M., Feignier, B., Bouchon, M., and Bethoux, N., 1993, Attenuation of crustal waves across the Alpine range, *J. Geophys. Res.* 98, 1987-1996.

Cormier, V.F. and Anderson, T., 1996, Lg blockage and scattering at CNET and KEET, *Proceedings of the 18th Annual Seismic Research Symposium on Monitoring a Comprehensive Nuclear-Test-Ban Treaty*, 159-168.

Cormier, V.F. and Anderson, T., 1997, Lg blockage and scattering at Central Eurasian Arrays CNET and ILPA, *Proceedings of the 19th Annual Seismic Research Symposium on Monitoring a Comprehensive Nuclear-Test-Ban Treaty*, 479-485, September 23-25.

Day, S.M. and K.L. McLaughlin, 1991, Seismic source representations for spall, Bull. Seism. Soc. Am., 81, 191-201.

De Wolf, D.A., 1971, Electromagnetic reflection from an extended turbulent medium: cumulative forward-scatter single-backscatter approximation, *IEEE trans. Ant. and Propag.*, AP-19, 254-262.

De Wolf, D.A., 1985, Renormalization of EM fields in application to large-angle scattering from randomly continuous media and sparse particle distributions, *IEEE trans. Ant. and Propag.*, AP-33, 608-615.

Fan, G.W. and T. Lay, 1998a, Statistical analysis of irregular waveguide influences on regional seismic discriminants in China, *Bull. Seismol. Soc. Am.*, 88, 74-88.

Fan, G.W. and T. Lay, 1998b, Regionalized versus single-station wave-guide effects on seismic discriminants in western China, *Bull. Seismol. Soc. Am.*, 88, 1260-1274.

Fan, G.W. and T. Lay, 1998c, Statistical analysis of irregular waveguide influences on regional seismic discriminants in China: additional results for Pn/Sn, Pn/Lg and Pg/Sn, *Bull. Seismol. Soc. Am.*, 88, 1504-1510.

Fan, G., T. Lay and S. Bottone, 2002, Path corrections for source discriminants: A case study at two international seismic monitoring stations, PAGEOPH, *Pure appl. Geophys.*, 159, 651-678.

Fisk, M. D., H. L. Gray and G. D. McCartor 1996, Regional discrimination without transporting thresholds, *Bull. Seism. Soc. Am.*, 86, 1545-1558.

Frankel, A. & Clayton, R.W., 1986. Finite-difference simulations of seismic scattering: Implications for propagation of short-period seismic waves in the crust and models of crustal heterogeneity, *J. Geophys. Res.*, 91, 6465-6489.

Frankel, A., 1989, A review of numerical experiments on seismic wave scattering, in *Scattering and Attenuation of Seismic Waves, II*, edited by R.S. Wu and K. Aki, pp. 639-686, Birkhauser, Berlin.

Fu, L.Y., 1996. 3-D boundary element seismic modeling in complex geology, *66th Ann. Internat. Mtg., Soc. Expl. Geophys., Expanded Abstracts*, 1239-1242.

Fu, L.Y. and Mu, Y.G., 1994. Boundary element method for elastic wave forward modeling: *Acta Geophys. Sinica*, 37, 521-529.

Fu, L.Y. and Wu, R.S., 2000. Infinite boundary element absorbing boundary for wave propagation simulations, *Geophysics*, 65, 625-637.

Fu, L.Y. and Wu, R.S., 2001. A hybrid BE-GS method for modeling regional wave propagation, Pure and Applied *Geophysics*, 158, 1251-1277.

Fu, L.Y., Wu, R.S. and Campillo, M., 2002, Energy partition and attenuation of regional phases by random free-surface, *Bull. Seis. Soc. Am.*, 92, 1992-2007.

Furumura, T. and Kennett, B.L.N., 1997, On the nature of regional seismic phases -II. On the influence of structural barriers, *Geophys. J. Int.*, 129, 221-234.

Gibson, Jr, R.L. and Campillo, M., 1994. Numerical simulation of high- and low-frequency Lg-wave propagation, *Geophys. J. Int.*, 118, 47-56.

Goff, J.A. and K. Holliger, (editors), 2002, Characterization in the *Crust and Upper Mantle: Nature, Scaling and Seismic Properties*, Kluwer Academic, New York.

Goldstein, P., Bhattacharyya, J., Ichinose, G., Leach, R., 1999, On the sensitivity of broad band regional seismic phases to multi-dimensional earth structure: Implications for phase identification, *Proceedings of the 21st Annual Seismic Research Symposium on Monitoring a Comprehensive Nuclear-Test-Ban Treaty*, 58-63, September 21-24.

Goldstein, P., Schultz, C., Larsen S., and Minner, L., 1996, Modeling of regional wave propagation phenomena in the middle east and north Africa and new analysis capabilities in SAC2000, *Proceedings of the 18th Annual Seismic Research Symposium on Monitoring a Comprehensive Nuclear-Test-Ban Treaty*, 165-171, September 4-6.

Goldstein, P., Schultz, C., and Larsen S., 1997, The influence of deep sedimentary basins, crustal thinning, attenuation, and topography on regional phases: Selected examples from the Eastern Mediteranean and the Caspian sea regions, *Proceedings of the 19th Annual Seismic Research Symposium on Monitoring a Comprehensive Nuclear-Test-Ban Treaty*, 486-494, September 23-25.

Gupta, I.N., W. Chan, and R. Wagner, 1992, A comparison of regional phases from underground nuclear explosions at East Kazakh and Nevada Test Sites, *Bull. Seism. Soc, Am.*, 82, 352-382.

Gupta, I. N., T. Zhang, and R. A. Wagner 1997, Low-frequency Lg from NTS and Kazakh nuclear explosions: observations and interpretations, *Bull. Seism. Soc. Am.*, 87, 1115-1125.

Gutowski, P.R., Hron, F., Wagner, D.E. and Treitel, S., 1984, S*, *Bull. Seism. Soc. Am.* 74, 61-78.

Hartse, H.E., S.R., Taylor, W.S., Phillips, and G.E., Randall, 1997, A preliminary study of regional seismic discrimination in central Asia with emphasis on western China, *Bull. Seism. Soc. Am.*, 87, 551-568.

Herrmann, R.B., Mokhtar, T.A., Raoof, M., and Ammon, C., 1997, Wave propagation-16Hz to 60 sec, *Proceedings of the 19th Annual Seismic Research Symposium on Monitoring a Comprehensive Nuclear-Test-Ban Treaty*, 495-503, September 23-25.

Huang, L.J., Fehler, M.C., Wu, R.S., 1999, Extended local Born Fourier migration method, *Geophysics*, 64, 1524-1534.

Huang, L.J., Fehler, M.C., Roberts, P.M., and Burch, C.C., 1999, Extended local Rytov Fourier migration method, *Geophysics*, 64,1535-1545.

Huang, L.J. and Wu, R.S., 1996, *3D prestack depth migration with acoustic pseudo-screen propagators, Mathematical methods in geophysical imaging IV, SPIE*, 2822, 40-51.

Husebye, E.S. and Ruud, B.O., 1996, Wave propagation in complex crust- CTBT implications, *Proceedings of the 18th Annual Seismic Research Symposium on Monitoring a Comprehensive Nuclear-Test-Ban Treaty, 172-181*, September 4-6.

Jih, R.S., 1995, Numerical investigation of relative contribution of Rg scattering and incomplete dissipation to Lg excitation, *Proceedings of the 17th Seismic Research Symposium on Monitoring a CTBT, PL-TR-95-2108.*

Jih, R.S., 1996, Waveguide Effects of large-scale structural variation, anelastic attenuation, and random heterogeneity on SV Lg propagation: a finite-difference modeling study, *Proceedings of the 18th Annual Seismic Research Symposium on Monitoring a Comprehensive Nuclear-Test-Ban Treaty*, 182-194, September 4-6.

Jin, S. and Wu, R.S., 1999, Depth migration with a windowed screen propagator, *Journal of Seismic Exploration*, 8, 27-38.

Jin, S., Wu, R.S., and Peng, C., 1999, Seismic depth migration with screen propagators, *Computational Geoscience*, 3, 321-335.

Johnson, L.R., and C.G. Sammis, 2001, Effects of rock damage on seismic waves generated by explosions, *Pageoph*, 158, 1869-1908.

Jones, E.M., App, F.N., and Bos, R.J., 1997, The effects of major structural features in Western China on explosion seismograms, *Proceedings of the 19th Annual Seismic Research Symposium on Monitoring a Comprehensive Nuclear-Test-Ban Treaty*, 504-513, September 23-25.

Jones, E.M. and Holliger, K., 1997, Spectral analyses of the KTB sonic and density logs using robust nonparametric methods, *J. Geophys. Res.*, 102, 18391-18403.

Keers, H., Nolet, G., and Dahlen, F.A., 1996a, Ray theoretical analysis of Lg, *Bull. Seis. Soc. Am.*, 86, 726-736.

Keers, H., Vogfjord, G., Nolet, G., and Dahlen, F.A., 1996b, High frequency propagation of crustal waves, *Proceedings of the 18th Annual Seismic Research Symposium o Monitoring a Comprehensive Nuclear-Test-Ban Treaty*, 199-205, September 4-6.

Kennett, B.L.N., 1984. Guided wave propagation in laterally varying media-I: Theoretical development, *Geophys. J. Roy. Astr. Soc.*, 79, 235-255.

Kennett, B.L.N., 1986, Lg waves and structural boundaries, *Bull. Seis. Soc. Am.*, 76, 1133-1141.

Kennett, B.L.N., 1989, Lg-wave propagation in heterogeneous media, Bull. Seis. Soc. Am., 79, 860-872.

Kennett, B.L.N., 1998, Guided waves in three-dimensional structures. *Geophys. J. Int.*, 133, 159-174.

Kennett, B.L.N., 1990, Guided wave attenuation in laterally varying media, *Geophys. J. Int.*, 100, 415-422.

Kennett, B.L.N., Bostock, M.G., and Xie, J.K., 1990, Guided-wave tracking in 3-D - A tool for interpreting complex regional seismograms, *Bull. Seis. Soc. Am.*, 80, 633-642.

Kim, W. Y., V. Aharonian, A. L. Lerner-Lam and P. G. Richards 1997. Discrimination of earthquakes and explosions in southern Russia using regional high-frequency three-component data from IRIS/JSP Caucasus Network, *Bull. Seism. Soc. Am.*, 87, 569-588.

Kim, W. Y., D. W. Simpson and P. G. Richards 1993. Discrimination of earthquakes and explosions in the eastern United States using regional high-frequency data, *Geophys. Res. Lett.*, 20, 1507-1510.

Hayashi, K., D.R. Burns, and M.N. Toksöz, 2001, Discontinuous-grid finite-difference seismic modeling including surface topography, *Bull. Seis. Soc. Am.*, 91, 1750-1764.

Kosloff, D. and E. Baysal, 1982, Forward modeling by a Fourier method, *Geophysics*, 47, 1402-1412.

Kosloff, D., Kessler, D., Quieroz, A., and Tessmer, E., 1990, Solution of the equations of Dynamic elasticity by a Chebychev spectral method, *Geophysics*, 55, 734-748.

Lay, T., Fan, G., Wu, R.S., and Xie, X.B., 1999, Path corrections for regional phase discriminants, *Proceedings of the 21st Annual Seismic Research Symposium on Monitoring a Comprehensive Nuclear-Test-Ban Treaty*, 510-519, September 21-24.

Maupin V., 1989, Numerical modeling of Lg wave propagation across the North Sea central graben, *Geophys. J. Int.*, 99, 273-283.

Maupin, V. and Kennett, B.L.N., 1987, On the use of truncated model expansion in laterally varying media, *Geophys. J. R. Astr. Soc.*, 91, 837-851.

McLaughlin, K.L. and Wilkins, D., 1997, Progress in numerical methods for wave propagation, *Proceedings of the 19th Annual Seismic Research Symposium on Monitoring a Comprehensive Nuclear-Test-Ban Treaty*, 514-523, September 23-25.

Morse, P.M. & Feshbach, H., 1953. *Methods of Theoretical Physics*, McGraw-Hill, New York.

Myers, S.C., J. Wagoner, S. Larsen, A. Rodgers, K. Mayeda, K. Smith, and W. Walter, 2003, Simulation of regional explosion S-phases (SIRES) project, *Proceedings of the 25th Seismic Research Review, Muclear Explosion Monitoring: Building the Knowledge Base*, 117-124.

Ni, J., Reese, C., Wu, J., and Zhao, L.S., 1996, Crustal structure and attenuation in Southern Tibet, *Proceedings of the 18th Annual Seismic Research Symposium on Monitoring a Comprehensive Nuclear-Test-Ban Treaty*, 390-399, September 4-6.

Nolte, B., Gibson, R.L., and Toksöz, M.N., 1996, Irregular-grid modeling of regional wave propagation, *Proceedings of the 18th Annual Seismic Research Symposium on Monitoring a Comprehensive Nuclear-Test-Ban Treaty*, 231-240, September 4-6.

Nuttli, O.W., 1986, Yield estimates of Nevada Test Site explosions obtained from Lg waves, *J. Geophys. Res.*, 91, 2137-2151.

Orrey, J., Archambeau, C., and Frazier, G., 2003, Complete seismic wave field synthesis with a pseudospectral method: The generalized Fourier method, submitted to *Geophys. J. Int.*

Priestley, K. F., G. Zandt, and G. E. Randall, 1988, Crustal structure in Eastern Kazakh, USSR from teleseismic receiver functions, *Geophys. Res. Lett.*, 15, 613-616.

Patton, H.J., 2001, Regional magnitude scaling, transportability, and Ms:mb discrimination at small magnitudes, *Pageoph*, 158, 1951—2015.

Sánchez-Sesma, F.J., Bravo, M.A., and Herrera, I., 1985. Surface motion of topographical irregularities for incident P, SV, and Rayleigh waves, *Bull. Seis. Soc. Am.*, 75, 263-269.

Sánchez-Sesma, F.J. & Campillo, M., 1991. Diffraction of P, SV and Rayleigh waves by topographic features: a boundary integral formulation, *Bull. Seis. Soc. Am.*, 81, 2234-2253.

Sato, H. and Fehler, M.C., 1998, *Seismic Wave Propagation and Scattering in the eterogeneous Earth*, Springer-Verlag New York, Inc.

Schatzman, J.C., 1996, A pseudo-spectral scheme for viscoelastic seismic modeling, *roceedings of the 18th Annual Seismic Research Symposium on Monitoring a Comprehensive Nuclear-Test-Ban Treaty*, 261-270, September 4-6.

Stevens, J.L., G.E. Baker, H. Xu, T.J. Bennett, N. Rimer, S.M. Day, 2003, The physical basis of Lg generation by explosion sources, *Proceedings of the 25th Seismic Research Review, Muclear Explosion Monitoring: Building the Knowledge Base*, 456-465.

Taylor, S.R., 1996, Analysis of high frequency P_n/L_g ratios from NTS explosions and western U.S. earthquakes, *Bull. Seism. Soc. Am.*, 86, 1042-1053.

Taylor, S. R., M. D. Denny, E. S. Vergino, and R. E. Glaser 1989, Regional discrimination between NTS explosions and western U.S. earthquakes, *Bull. Seism. Soc. Am.*, 79, 1142-1176.

Taylor, S. R., and H. E. Hartse, 1997. An evaluation of generalized likelihood ratio outlier detection to identification of seismic events in western China, *Bull. Seism. Soc. Am.*, 87, 824-831.

Tessmer, E. and D. Kosloff, 1994, 3-D elastic modeling with surface topography by a Chebychev spectral method, *Geophysics*, 59, 464-473.

Vidale, J.E. and D.V. Helmberger, 1988, Elastic finite-difference modeling of the 1971 San Fernando, California earthquake, *Bull. Seism. Soc. Am.*, 78, 122-144.

Vogfjord, K.S., 1997, Effects of explosion depth and earth structure on the excitaion of Lg waves: S* revisited, *Bull. Seism. Soc. Am.*, 87, 1100-1114.

Wallace, T.C., 1991, Body wave observations of tectonic release, in: S.R. Taylor, H.J. Patton and P.G. Richards (editors), *Explosion Source Phenomenology*, pp 161-170, American Geophysical Union.

Walter, W.R., K.M., Mayeda, and H. Patton, 1995, Phase and spectral ratio discrimination between NTS earthquakes and explosions. Part I: Empirical observations, *Bull. Seism. Soc. Am.*, 85, 1050-1067.

Wild, A.J. and Hudson, J.A., 1998, A geometrical approach to the elastic complex screen, *J. Geophys. Res.*, 103, 707-725.

Wu, R.S. and K. Aki (editor), 1988, *Scattering And Attenuation Of Seismic Waves, Volume I*, Birkhauser Verlag, Boston.

Wu, R.S. and K. Aki (editor), 1989, *Scattering And Attenuation Of Seismic Waves, Volume II*, Birkhauser Verlag, Boston.

Wu, R.S. and K. Aki (editor), 1990, *Scattering And Attenuation Of Seismic Waves, Volume III*, Birkhauser Verlag, Boston.

Wu, R.S., 1989. Representation integrals for elastic wave propagation containing either the displacement term or the stress term alone, Physical Rev. Letters, 62, 497-500.

Wu, R.S., 1994, Wide-angle elastic wave one-way propagation in heterogeneous media and an elastic wave complex-screen method, *J. Geophys. Res.*, 99, 751-766.

Wu, R.S., 1996, Synthetic seismograms in heterogeneous media by one-return approximation, *Pure and Applied Geophysics*, 148, 155-173.

Wu, R.S., and Huang, L.J., 1995, Reflected wave modeling in heterogeneous acoustic media using the de~Wolf approximation, *Mathematical Methods in Geophysical Imaging-III, SPIE Proceedings Series*, 2571, 176-186.

Wu, R.S., Huang, L.J., and Xie, X.B., 1995, Backscattered wave calculation using the De Wolf approximation and a phase-screen propagator, *Expanded Abstracts, SEG 65th Annual Meeting*, 1293-1296.

Wu, R.S., S. Jin, and X. B. Xie, 1996. Synthetic seismograms in heterogeneous crustal waveguides using screen propagators, *Proceedings of the 18th Annual Seismic Research Symposium on Monitoring a Comprehensive Test Ban Treaty*, 290-300.

Wu, R.S., S. Jin and X.B. Xie, 2000a, Seismic wave propagation and scattering in heterogeneous crustal waveguides using screen propagators: I SH waves, *Bull. Seism. Soc. Am.*, 90, 401-413.

Wu, R.S., S. Jin and X.B. Xie, 2000b, Energy partition and attenuation of Lg waves by numerical simulations using screen propagators, *Phys. Earth and Planet. Inter.*, 120, 227-243.

Wu, R.S. and Xie, X.B., 1994, Multi-screen backpropagator for fast 3D elastic prestack migration, *Mathematical Methods in Geophysical Imaging-II, SPIE Proceedings Series*, 2301, 181-193.

Wu, R. S., Xie, X. B., Jin, S., Fu, L., and Lay, T., 1998. Seismic wave propagation and scattering in heterogeneous crustal waveguides using screen propagators, *Proceedings of the 20th Annual Seismic Research Symposium on Monitoring a Comprehensive Nuclear-Test-Ban Treaty*, 201-210.

Wu, R.S., X.B. Xie, and X.Y. Wu, 1999. Lg wave simulations in heterogeneous crusts with irregular topography using half-space screen propagators, *Proceedings of the 21th Annual Seismic Research Symposium on Monitoring a Comprehensive Test Ban Treaty*, 683-693.

Wu, R.S., Xie, X.B., and Wu, X.Y., 2000, Lg wave propagation using SH and P-SV screen propagators in heterogeneous crusts with irregular topography, *Proceedings of the 22nd Annual Seismic Research Symposium on Monitoring a Comprehensive Nuclear-Test-Ban Treaty.*

Wu, R.S., X.B. Xie, X.Y. Wu, and Lay T., 2002. Quantifying source excitation and path effects for high-frequency regional waves. *Proceedings of the 24th Annual Seismic Research Symposium on Monitoring a Comprehensive Test Ban Treaty*, 209-218.

Wu, R.S., X.B. Xie, X. Wu and T. Lay, 2003, Quantifying source excitation and path effects for high frequency regional waves, *Proceedings of the 25th Seismic Research Review, Muclear Explosion Monitoring: Building the Knowledge Base*, 173-181.

Wu, R.S., X.B. Xie, Z. Ge and T. Lay, 2004, Quantifying source excitation and path effects for high frequency regional waves, *Proceedings of the 26th Seismic Research Review, Muclear Explosion Monitoring: Trends in Nuclear Explosion Monitoring*, 191-201.

Wu, R.S., Xu, Z., and Li, X.P., 1994, Heterogeneity spectrum and scale-anisotropy in the upper crust revealed by the German continental deep-drilling (KTB) holes, *Geophysi. Res. Lett.*, 21, 911-914.

Wu, X.Y., and R.S. Wu, 2001. Lg wave simulations in heterogeneous crusts with irregular topography using halfspace screen propagators, *Geophys. J. Int.*, 146, 598-606.

Xie, J., 1998, Spectral inversion using Lg from earthquakes: improvement of the method with applications to the 1995, western Texas earthquake sequence, *Bull. Seism. Soc. Am.*, 88, 1525-1537.

Xie, J., 2002, Lg Q in the eastern Tibetan Plateau, *Bull. Seism. Soc. Am.*, 92, 871-876.

Xie, J., Cong, L.L., and Mitchell, B.J., 1996, Spectral characteristics of the excitation and propagation of Lg from underground nuclear explosions in central Asia, *J. Geophys. Res.*, 101, 5813-5822.

Xie, J. and Patton, H.J., 1999, Regional phase excitation and propagation in the Lop Nor region of central Asia and inplications for P/Lg discriminations, *J. Geophys. Res.*, 104, 941-954.

Xie, X.B. and Lay, T., 1994, The excitation of Lg waves by explosions: A finite-difference investigation, *Bull. Seism. Soc. Am.*, 84, 324-342.

Xie, X.B. and Wu, R.S., 1995, A complex-screen method for modeling elastic wave reflections, *Expanded Abstracts, SEG 65th Annual Meeting*, 1269-1272.

Xie, X.B. and Wu, R.S., 1996, 3D elastic wave modeling using the complex screen method, *Expanded Abstracts, SEG 66th Annual Meeting*, 1247-1250.

Xie, X.B. and Wu, R.S., 1998, Improving the wide angle accuracy of the screen method under large contrast, *Expanded Abstracts, SEG 68th Annual Meeting*, 1811-1814.

Xie, X.B. and Wu, R.S., 1999, Improving the wide angle accuracy of the screen propagator for elastic wave propagation, *Expanded Abstracts, SEG 69th Annual Meeting*, 1863-1866.

Xie, X.B. and Wu, R.S., 2001, Modeling elastic wave forward propagation and reflection using the complex-screen method, *J. Acoust. Soc. Am.*, 109, 2629-2635.

Xie, X.B. and Wu, R.S., 2004, Multicomponent prestack depth migration using the elastic screen method, *Geophysics*, in press.